

**Numerical Predictions of Propeller-Wing Interaction Induced Noise
in Cruise and Off-Design Conditions**

by

David A. Boots, B. Eng.

Carleton University

A thesis submitted to
the Faculty of Graduate Studies and Research
in partial fulfillment of
the requirements for the degree of

Master of Applied Science

Ottawa-Carleton Institute for
Mechanical and Aerospace Engineering

Department of
Mechanical and Aerospace Engineering

Carleton University

Ottawa, Ontario

July 2016

© Copyright

2016 – David A. Boots

Abstract

Using numerical methods, the aeroacoustic field induced by the interaction of a 4-bladed NASA SR-2 propeller and its wake with a wing is investigated under cruise conditions (Mach 0.6). The SmartRotor code, a coupled vortex particle and panel method, which is integrated with an acoustic solver based on the Farassat 1A formulation of the Ffowcs-Williams Hawkins equation, was used. Three main areas were investigated: the effect of propeller tip geometry on the propeller's wake and blade tip vortex; the effect of integrating a wing in the tractor configuration, including the effect of its position, and wing local leading edge sweep; and the effect of operating the combined wing/propeller system in off-design conditions such as low forward speed or in non-axial inflow.

It was discovered that tip sweep is effective at reducing propeller tip vortex strength with no adverse effect on noise. Modifying tip dihedral was found to always increase tip vortex strength. Integrating a wing in the wake of the propeller increased the broadband noise generated, but had little effect on harmonic noise. The downstream position of the wing was found to not affect noise while vertical offset from the propeller axis increased noise. The most important discovery was that applying local leading edge sweep to the wing in the region of the propeller's wake decreases noise proportionally to the change in the angle between the helical tip vortex and the wing's leading edge. These noise reductions were on the order of up to 1.3 dB for overall sound pressure level, and 7.5 dB at the blade passage frequency.

Acknowledgements

First on the list of many people to thank must be my supervisor, Professor Daniel Feszty. His constant enthusiasm and support of my work was invaluable whenever simulations weren't working or results seemed less than reasonable. At the same time, his way of providing guidance while allowing me to choose the direction of my research allowed me to follow up on interesting results and truly take ownership of this work. For this and so much more, thank you.

I also appreciate the endless support from my family: my parents, for inevitably asking about my thesis every Skype call and encouraging me at every opportunity; my brothers and sister, for at least pretending to be interested in my work and giving me plenty of opportunities to practice explaining my research. My siblings also encouraged me by their own successes, as with the completion of this thesis I will finally join the rest of them with graduate degrees.

My office-mates of Minto 3041 also deserve a shout-out for being fantastic friends and pranksters. Being surrounded by such awesome people made all those hours of research fly by. My research partner, Jason, deserves a special thank-you for calling out my errors, offering suggestions, and being a great sounding board. Finally, I must acknowledge all my other friends in Ottawa: having such a positive experience these last two years has helped me stay motivated and focused.

Finally, this work was financially supported by a research grant provided by the Green Aviation Research and Development Network (GARDN) and Pratt & Whitney Canada.

Contents

Abstract	ii
Acknowledgements	iii
Contents	iv
List of Tables	vi
List of Figures	vii
List of Symbols	x
Aerodynamic	x
Acoustic	xi
1. Introduction	1
1.1. Background	1
1.2. Fundamentals of Propeller Acoustics	2
1.3. Literature Review	6
1.3.1. Propeller Tip Vortex	6
1.3.2. Propeller Wake-Wing Interaction	7
1.3.3. Full Configuration	10
1.4. Motivation	11
1.5. Objectives	13
1.6. Thesis Overview	14
2. Simulation Methodology	16
2.1. Research Methodology	16
2.2. Test Cases	17
2.3. Numerical Method	20
2.3.1. SmartRotor Aerodynamic Component	20
2.3.2. SmartRotor Aeroacoustic Component	29
2.3.3. Modifications to the SmartRotor Code	35

2.4. Verification	37
2.5. Aerodynamic Validation	41
2.6. Aeroacoustic Validation	43
2.7. Summary of SmartRotor Capabilities and Limitations	47
3. Effect of Tip Shape on Vortex Structure	49
3.1. General Setup	49
3.2. Effect of Tip Leading Edge Sweep	52
3.3. Effect of Tip Dihedral	54
3.4. Effect of Tip Twist	56
4. Effect of Propeller Vortex-Wing Interference on Noise.....	60
4.1. Background	60
4.2. Baseline Results	62
4.3. Effect of Tip Vortex Strength	66
4.4. Effect of Wing Placement	67
4.5. Effect of Wing Local Leading Edge Sweep	71
4.6. Effect of Complete Propeller, Nacelle, Wing Configuration	76
5. Effect of Off-Design Conditions on Noise	79
5.1. Background	79
5.2. Effect of Non-Axial Inflow	80
5.2.1. Angle of Attack	80
5.2.2. Yaw Angle	81
5.2.3. No Forward Speed.....	82
6. Recommendations and Conclusions.....	85
6.1. Conclusions	85
6.2. Recommendations for Future Work.....	87
References	91

List of Tables

Table 1. Validation Test Matrix.....	18
Table 2. Aerodynamic validation test parameters.....	42
Table 3. Aerodynamic validation results.....	43
Table 4. Aeroacoustic validation test setup.....	44
Table 5. Parametric study parameters and ranges.....	51

List of Figures

Figure 1. Schematic of air particles and their motion in a plane wave forced by the oscillating surface	2
Figure 2. Typical human hearing equal perceived loudness curves with typical propeller frequency range highlighted.....	3
Figure 3. Technical drawing of the NASA SR-2 propeller.....	19
Figure 4. Propeller geometry curves of the SR-2 propeller used for the test case.....	19
Figure 5. SR-2 geometry and axis convention	20
Figure 6. Example surface discretization	26
Figure 7. The formation of vortex particles from a trailing edge wake strip	29
Figure 8. Physical meaning of the sources seen in the FW-H equation.....	31
Figure 9. Mesh distribution on a blade.....	38
Figure 10. Grid convergence results for spanwise elements and chordwise elements....	39
Figure 11. Time step size and simulation length convergence results	39
Figure 12. Example acoustic pressure time history with rejected regions highlighted	40
Figure 13. Resulting frequency spectrum from the example time history	41
Figure 14. Wake visualization after three revolutions.....	43
Figure 15. SmartRotor acoustic results.....	45
Figure 16. Acoustic spectra showing the effect of wind tunnel background noise	46
Figure 17. Sweep and dihedral displacement examples.....	50
Figure 18. Propeller, wake, and microphone location.....	51
Figure 19. Sweep parametric study geometry curves	52
Figure 20. Sweep parametric study results	53
Figure 21. Dihedral parametric study geometry curves	54
Figure 22. Dihedral parametric study results	55

Figure 23. Comparison of wake structure for tip dihedral +40 degrees and -40 degrees.....	56
Figure 24. Twist parametric study results with linear twist change	57
Figure 25. Twist parametric study geometry curves with linear twist change	58
Figure 26. Twist parametric study geometry curves with parabolic twist change	58
Figure 27. Twist parametric study results with parabolic twist change	59
Figure 28. Illustration of the effect of wing vertical position on vortex impact angle.....	61
Figure 29. Wake particle visualization of the baseline WVI case.....	63
Figure 30. Comparison of WVI baseline case and isolated propeller	64
Figure 31. Front view of the developed wake showing the flattening effect of the wing surface	65
Figure 32. Wing/propeller mutual interference effects	65
Figure 33. Effect of propeller tip twist on WVI noise at the baseline wing position	66
Figure 34. Effect of tip twist on noise at a vertical position of 1.0R	67
Figure 35. Wing leading edge position downstream and vertical range	68
Figure 36. Effect of wing downstream position on noise	69
Figure 37. Effect of wing vertical position on noise.....	70
Figure 38. OASPL and 1HSPL change with wing position from baseline case.....	71
Figure 39. Leading edge shapes.....	72
Figure 40. Effect of leading edge shape on noise with wing on propeller axis.....	73
Figure 41. Effect of leading edge shape on noise with wing 0.5R above the propeller axis... ..	74
Figure 42. Shifting of sound pressure level to the second harmonic seen with high LE sweep.....	75
Figure 43. Effect of leading edge shape on noise with wing 1.0R above the propeller axis... ..	76
Figure 44. Full configuration wake visualization.....	77

Figure 45. Acoustic spectrum of full configuration.....	78
Figure 46. Acoustic spectrum of varying angles of attack	81
Figure 47. Acoustic spectrum of varying yaw angles	82
Figure 48. Acoustic spectrum at zero forward speed compared to that at cruise	84
Figure 49. Particle wake structure at zero forward speed and at cruise	84

List of Symbols

Aerodynamic

$[C^{\text{Lifting}}_{ij}]$	Influence coefficient matrix for lifting body elements (evaluated at panel control points)
$[C^{\text{Near wake}}_{ik}]$	Influence coefficient matrix for near wake elements (evaluated at panel control points)
$[C^{\text{Non-lifting}}_{il}]$	Influence coefficient matrix for non-lifting body elements (evaluated at panel control points)
C_p	Pressure coefficient
D_ω	Domain for far wake (vorticity) calculations
F	Local normal velocity due to surface motion and far wake induced velocity
F_i	Local normal velocity for panel element i
$f_\varepsilon(\)$	Beale and Majda vortex 'blob' function (eq. (2.17))
\vec{n}	Local outward normal unit vector
\vec{P}	Evaluation point
R_j	Distance from a given vortex particle to the evaluation point
r	Distance from a given element to the evaluation point
S	Surface over which to integrate
t	Time
\vec{u}	Total flow velocity
\vec{u}_{ext}	Externally-induced flow velocity
$\vec{u}_{\text{far wake}}$	Far wake-induced flow velocity
$\vec{u}_{\text{near wake}}$	Near wake-induced flow velocity
\vec{u}_{panel}	Panel-induced flow velocity
\vec{u}_{solid}	Solid panel-induced flow velocity
u	Local flow velocity magnitude
u_{ref}	Reference flow velocity
$\{u_j\}$	Vector of resultant velocities induced by lifting bodies
$\{u_k\}$	Vector of resultant velocities induced by near wake elements
\vec{x}	Position vector
\vec{x}_0	Position vector of a point of a vortex
\vec{Z}_j	Position vector of a vortex particle
$\delta(\)$	Dirac delta function
ε	Vortex particle cut-off length

σ	Local source intensity
$\{\sigma_i\}$	Vector of resultant source intensities of non-lifting bodies
ϕ	Scalar velocity potential
$\vec{\Omega}_j$	Vorticity of a given vortex particle
$\vec{\omega}$	Vorticity

Acoustic

c	Speed of sound
f	Force applied to a given fluid element (i.e. loading)
$H(\)$	Heaviside Function
l_i	Loading on an element
\dot{l}_i	Time derivative of the loading on an element
l_r	Loading on an element in the direction of noise radiation (towards the microphone)
M_i	Mach number of the velocity of an element
\dot{M}_i	Time derivative of the Mach number of the velocity of an element
M_r	Mach number of the velocity of an element in the direction of noise radiation (towards the microphone)
n	Number of samples in the pressure-time history
n_i	Local normal unit vector
p'	Total acoustic pressure
p'_{Loading}	Acoustic pressure induced by loading sources
$p'_{\text{Thickness}}$	Acoustic pressure induced by thickness sources
p'_{ref}	Reference acoustic pressure
p'_t	Acoustic pressure at a given time sample
\vec{r}	Vector from the noise source to the observer
r	Magnitude of the vector from the noise source to the observer
S	Surface over which to integrate
T_{ij}	Lighthill stress tensor
t	Time
t_1	Starting time of acoustic sampling
t_2	Ending time of acoustic sampling
\vec{u}_∞	Velocity of undisturbed flow
v_i	Velocity of the flow at a given point
v_n	Velocity of the flow normal to a given point
\vec{x}	Position of the observer

\vec{y}	Position of an acoustic source
$\delta(\)$	Dirac delta function
ρ_0	Density of undisturbed medium

1. Introduction

1.1. Background

Since the dawn of aviation, propellers have been essential to air travel. Their ability to efficiently convert the rotational motion of an engine into a forward force allowed for humanity to counter drag in the same way as wings allowed us to overcome gravity. Aircraft propellers can be classified into three categories based on their drive system, which determines their operating conditions. Piston propellers typically operate at up to 3000 RPM and are fixed to the engine shaft so they rotate at the same velocity. Turbopropellers, which will be the focus of this work, typically operate between 900 and 2500 RPM and are driven by a turbine via a reduction gearbox. The last category, propfans, are mostly experimental and operate at higher rotational speeds, often with the blade tips operating supersonically.

As ubiquitous as are propellers is the recognizable sound that accompanies them. The noise generated by propellers has long been a subject of research [1]–[15], especially after the rise of turbopropellers and during the investigation of high-speed propfans. Spinning at faster speeds and generating more thrust leads to greater noise being emitted and so the effort to reduce propeller noise is more salient than ever. While recent years have seen turbopropeller aircraft begin to take back market share from jet aircraft due to their greater fuel economy and superior short-haul performance [16], increasingly restrictive noise regulations have somewhat hampered their rise so the industry has rekindled interest in propeller noise reduction. The general

purpose of this work is to further enhance the understanding of propeller noise for turboprop aircraft.

1.2. Fundamentals of Propeller Acoustics

Before describing the means by which a propeller creates noise, it is worthwhile to briefly examine the nature of sound and noise. Sound is the propagation of oscillating pressure waves through the air. These oscillations transport very little mass but rather vibrate individual fluid particles as the pressure variation travels in the form of a wave at the speed of sound. The difference between what we refer to as acoustic pressure and normal pressure is that the variations in acoustic pressure are at a much higher frequency and have no effect on flow characteristics due to their significantly lower magnitude.

Figure 1 demonstrates how regions of high acoustic pressure travel to neighbouring regions only to be drawn back by low pressure on the other side. So sound is, in effect, any periodic fluctuation of acoustic pressure.

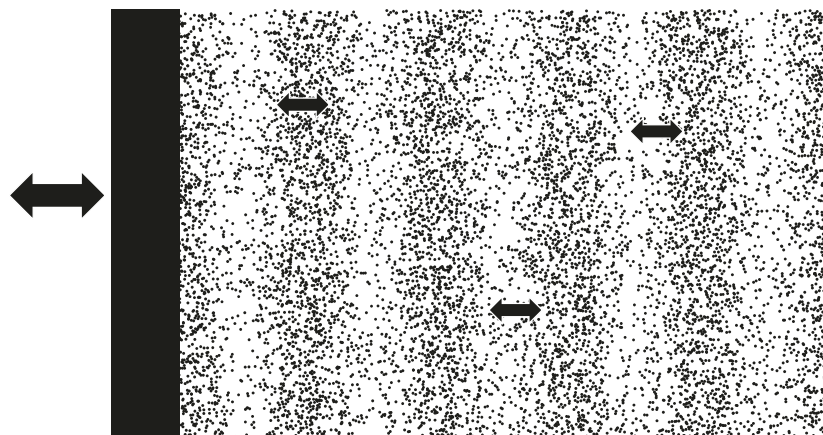


Figure 1. Schematic of air particles and their motion in a plane wave forced by the oscillating surface.

As sound is a wave, it is often best described in the frequency domain as opposed to the time domain. There are three main ranges of frequency, based on the ability of humans to perceive the noise. Infrasonic is the range of frequencies below which humans can hear. This range is important in the study of comfort and human factors as the upper range can be consciously felt and the whole range can lead to discomfort. Next is the sonic range, from approximately 20 Hz to 20 kHz. The ability of humans to hear this noise is slightly lower at the bottom range, peaks at about 5000 Hz, and then decreases beyond that. Figure 2 shows the typical perceived noise level compared to the true sound pressure level. Finally, there is the ultrasonic range, which is above the range humans can hear, and is important for the study of material fatigue.

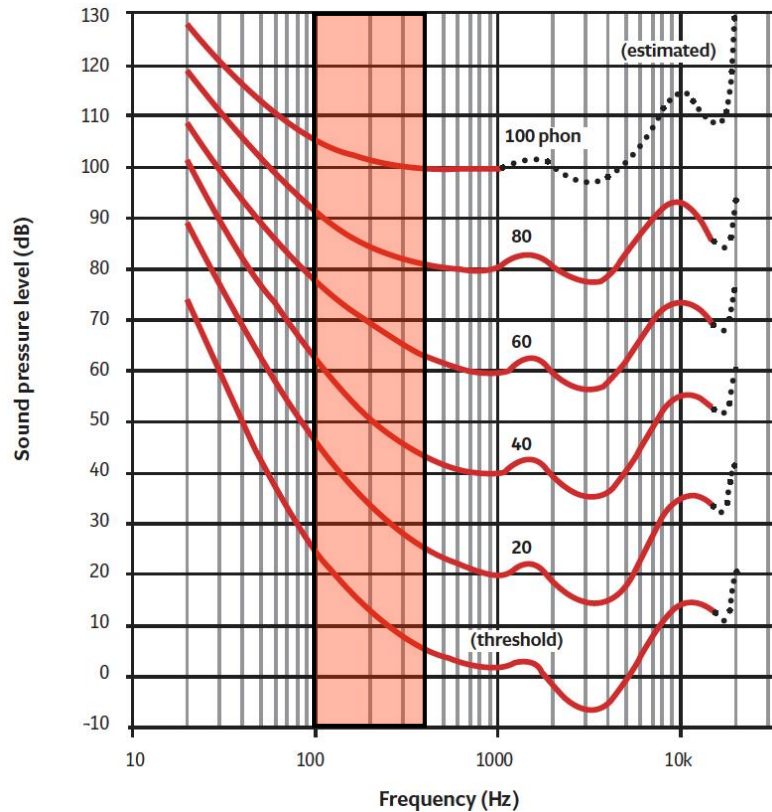


Figure 2. Typical human hearing equal perceived loudness curves with typical propeller frequency range highlighted [17].

The mechanisms by which propellers generate noise have been well documented since the earliest investigations into propeller noise [1]–[4]. The primary mechanisms of propeller noise production are thrust, torque, thickness, and vortex shedding [1], [2], [4].

Thrust and torque are often grouped together as loading noise because they both stem directly from the pressure loads on the blade. Loading noise is the most significant source of noise under most operating conditions. When rotating, the blades of the propeller develop a pressure distribution around the airfoil due to the relative movement of the fluid. This pressure field is harnessed to generate thrust as the air has an equal and opposite force applied to it. It can be decomposed into the thrust component, in the direction of the propeller axis, and a torque component, in the direction of rotation. While the pressure field is roughly constant through time relative to the blade, to a stationary observer it translates from a steady pressure in the rotating frame to a periodic fluctuation. This apparent periodic fluctuation in pressure is, by definition, noise in the stationary reference frame with a frequency equal to the rate at which blades pass a given point on the propeller disc. This sort of noise that is generated at the same frequency as the blade passage frequency is termed ‘tonal’ or ‘harmonic’ noise in propeller acoustics. Unfortunately, as thrust and torque are essential to the operation of a propeller, this mechanism can only be mitigated and not eliminated completely.

Thickness noise is caused by the movement of the blade through the fluid. As the blade passes, the fluid must separate and move out of the way. This leads to a region of high pressure at the leading edge and a region of lower pressure at the trailing edge. Although these regions are, again, steady relative to the blade, in the stationary frame they become a periodic oscillation in pressure with the same frequency as loading noise.

The fourth mechanism of noise production is vortex shedding and Mach quadrupole noise. The chaotic motion of air in the tip vortex and wake contribute to the noise field by the shear forces applied by one fluid particle on an adjacent one. These forces are significantly lower than those applied by thickness and loading. Finally, any shockwaves generated by transonic flow (i.e. near the propeller's tip) also create sharp pressure changes that translate to noise. For subsonic tip speeds, both of these mechanisms are significantly quieter than thickness and loading and are often ignored. These four mechanisms will be discussed further in Chapter 2.3.2 as they relate to the equations used in their calculation and an illustration of their physical meanings can be seen then (Figure 8).

Despite the body of research on the subject, a definitive analytical model of propeller noise remains elusive. Gutin [1] developed an analytical model to describe the thrust and torque noise of a propeller given certain approximations. Deming [2] later extended this method to include thickness noise. Various empirical models, each of which is tailored to certain applications, have described the more complex noise sources, but none have proved reliably accurate. The bulk of aeroacoustic prediction is

done by computational aeroacoustics in tandem with computational fluid dynamics. The methods used for this will be discussed in Section 2.3.2.

Another source of noise that has been less studied but is thought to contribute to noise, particularly cabin noise, is the interaction of the propeller's wake, especially the tip vortex, with the wing in the typical tractor configuration of the propeller-engine-wing integration. The periodic interaction of the tip vortex with the wing generates fluctuating pressure loads on the wing that translate into noise. They also may excite the skin and structure of the wing and propagate through the aircraft structure into the fuselage where they are re-emitted by the sidewalls into the cabin [18], [19].

1.3. Literature Review

In the following section a detailed literature review is provided to understand the state-of-the-art in the fields relevant to the current work.

1.3.1. Propeller Tip Vortex

Hanson [20] used analytical methods to investigate the effect of various propeller design parameters on the noise of an isolated propeller. While no investigation was done on the tip vortex or wake formation, he found blade sweep could be used to create destructive interference between different stations along the blade, corroborated by Metzger and Rohrbach [21]. Hanson also concluded that anhedral and dihedral were largely ineffective, and that twist was able to trade off noise and aerodynamic efficiency.

Chang and Sullivan [22] also used analytical methods to optimize propeller blade twist. They analyzed proplets similar to the tip dihedral to be studied in the present work. Their work was followed upon by Cho and Lee [23] who studied the optimization of all blade shape parameters for aerodynamic, but not acoustic, performance. None of these references analyzed the wake or tip vortex in depth.

In conclusion, the aerodynamic and acoustic performance of isolated propellers has been thoroughly investigated. However, no literature is available on the effect of propeller blade geometry parameters on the wake or tip vortex formation or strength.

1.3.2. Propeller Wake-Wing Interaction

The suggestion that the propeller tip vortex's interaction with the wing could be a significant noise contributor was first raised by Miller et al. in 1981 [19]. They addressed the assumption that cabin noise is due solely to propeller noise passing through the fuselage sidewalls, instead suggesting that vibrations propagating through the aircraft structure from excitation of the wing skin could be re-emitted as noise into the cabin. They found that the core of the propeller tip vortex contained a pressure differential equivalent to 20 dB above the acoustic pressure striking the fuselage sidewalls. While the simulation used in the present research cannot model the structural excitation of the wing skin, instead it will investigate the aeroacoustic effect of the pressure and loading fluctuation on the wing surface.

Unruh [18], [24], [25] followed up on the work of Miller et al. by conducting extensive acoustic experiments on the noise transmitted through the wing structure

into the cabin. He confirmed that structure-borne noise is indeed a significant contributor to cabin noise. While not offering many useful conclusions to the present research on external noise, one significant finding was that interference noise has a tendency to decrease with increasing propeller-wing separation.

Durbin and Groeneweg [26] performed a rough analytical investigation of propeller-wing interaction noise from a purely loading perspective, neglecting the effects of the wake impinging on the wing. They found that the propeller blade is now operating in a non-uniform flow field due to the inflow angle generated by the wing. This non-uniformity changes the normally steady loads on the blades to a periodically fluctuating load that has an effect on noise comparable to, and sometimes larger than, the steady loads. They also found that the directivity of the propeller-generated noise changes with the addition of a wing. On the side where the blades approach the wing plane from above, noise is increased, and similarly decreased where the blades approach the wing plane from below. They explain this as a result of constructive and destructive interference, respectively, between steady and unsteady sources.

Rangwalla and Wilson [27] were the first to apply an unsteady, incompressible panel method to the problem of propeller-wing interference from an aerodynamic perspective. They used a combined panel/vortex wake model, similar to the numerical method to be applied in this thesis, to solve the flow around a two-bladed Clark Y propeller in front of a GAW-1 wing with good validation to experiment. Their investigation did not extend to aeroacoustics or the relative position of the wing.

Fratello et al. [28] conducted a similar series of simulations and equivalent experiments involving a four-bladed NACA 64A408 propeller and RA 18-43N1L1 profile wing. Their objective was to quantify the influence on both the wing and propeller as well as their wakes due to the mutual influence of both bodies. Again, no investigation on noise effects was made.

Marretta et al. [29], [30] also examined the flow field around an integrated propeller and wings of various planforms and aspect ratios. Using a hybrid free wake analysis method with boundary element method, they furthered previous research by analyzing the time-varying loading on the wing. In their early work, this was not evaluated in terms of noise, however in their later work [31] they applied an aeroacoustic code as a proof of concept for computational aeroacoustic prediction of propeller-wing interference noise. This proof of concept showed that methods similar to those used herein can predict noise of the kind investigated in this research but offered no insight into means of mitigating the noise.

Since then, little literature has been published on propeller-wing interaction both in terms of aerodynamics or aeroacoustics. The two exceptions include Akkermans et al. [32] who investigated the noise effect of a tractor propeller on a high-lift wing with a Coanda flap. They investigated several angles of attack but only one configuration. The other is Clair et al. [33] who investigated the potential of sinusoidal, wavy leading edges as a means of reducing turbofan turbulence-airfoil interaction noise

reduction. This is, in effect, alternating leading edge sweep angles. They reported sound pressure level decreases of 3-4 dB.

Other research has been conducted on propeller vortex interaction in the context of contra-rotating propellers [34], [35] but is only tangentially applicable to the current work.

The literature review of this area shows that although some work has been done, it appears that there is room for further research, especially in understanding the effect of wing position on noise.

1.3.3. Full Configuration

In 1981, Welge et al. [36] analyzed the effect of the engine nacelle on the flow field around the wing of a tractor configuration turboprop. Their experiments did not extend to the investigation of the effect on the acoustics. Their conclusions were simply that leading edge separation due to the nacelle was possible in certain configurations and conditions.

Tanna et al. [37] performed aeroacoustic wind tunnel testing of a Lockheed C-130 Hercules wing/nacelle/propeller combination as well as with just the nacelle and propeller. Tanna et al. identified the angle of attack and associated inflow distortion due to the wing as primary drivers of installation noise. Again, there is a gap in the ability to predict the impact on noise of integrated turbopropeller propulsion systems.

1.4. Motivation

As part of the certification process for modern aircraft, stringent noise testing is conducted. This poses a difficulty for aircraft and engine manufacturers as performance and cost must come first to be commercially competitive while noise often takes a lower priority. A better understanding of propeller noise and methods of controlling it can help the industry to design quieter airplanes from the outset.

For the operator and airport authority, quieter aircraft would mean noise abatement procedures can be simplified and have less impact on operations while maintaining a similar impact on nearby communities. This would have a beneficial economic impact on both parties as well as the community by both increasing the flow of passengers and goods and by stimulating the local economy.

In addition to the regulatory reasons to reduce propeller noise, ergonomic, health, and environmental benefits may be reaped from quieter propeller designs and acoustically sensitive propeller and engine integration. Research has shown that living near airport approach and departure paths can be correlated with several health issues [38]. The incidence of mental health consultations, cardiovascular disease, and perinatal health problems has been noted to increase in areas affected by aircraft [38]. The pathway for these health concerns is believed to be a combination of interrupted sleep and generally increased stress due to annoyance. Schoolchildren have also been found to have higher blood pressure and a decreased problem solving ability [38], [39].

Propellers that minimize noise in off-design conditions could help mitigate this by reducing the impact of climb noise on nearby populations.

Passengers and aircrew are likely the most directly affected by propeller noise. They are exposed for the duration of the flight at a very close range. To protect them from potentially damaging noise exposure and to improve their ergonomic situation, insulation is added to the cabin. Quieter engines and propellers would allow the amount of insulation necessary to be reduced, cutting the weight of the aircraft and improving range, fuel economy, and performance. Reducing the noise transmitted into the fuselage from the excitation of the wing structure from the propeller tip vortices would be especially effective. Quieter propeller blades and acoustically sensitive installation would improve passenger comfort and aircrew noise fatigue.

Beyond the acoustic benefits that can be attained, quieter propellers are likely to be more efficient as less energy is lost in the form of noise. Those with weaker tip vortices will especially be more efficient as they reduce the circulation dumped in the vortex and instead convert it into useful thrust. These improvements in efficiency will decrease the amount of fuel used for a given flight, saving operators money and reducing the environmental impact of the aircraft. Since turbopropeller aircraft are attractive to operators because of their superior efficiency compared to turbofans or turbojets, any further increase in efficiency and performance will serve to further increase their market share [16].

1.5. Objectives

Following the lack of comprehensive literature on the effect of the propeller tip vortex and the wing-vortex interaction (WVI) on noise, the specific objectives of the current work are threefold:

1. Investigate the effect of propeller tip geometric parameters including sweep, dihedral, and twist on the tip vortex strength and propeller noise for subsequent application.
2. Determine the noise impact of wing-vortex interaction as well as the complete propeller, nacelle, wing mutual interaction. Concurrently investigate the effect of the wing's leading edge sweep on this wing-vortex interaction noise.
3. Investigate the effect of off-design conditions on the tip vortex, wake shape, and propeller noise in regards to both the isolated propeller and complete propeller, nacelle, wing configuration.

The primary objective of this work is to determine the magnitude of noise reduction that is possible with proper mutual placement of the wing and propeller disk, and appropriate shaping of the wing in the propeller wake region. It is believed that the interaction of the propeller vortex with the wing contributes significantly to noise. By placing the wing in such a way that weaker sections of the wake pass over it and adjusting the relative angle of the wing's leading edge and the propeller tip vortex the magnitude of the interaction noise can be decreased. In the later stages of this work,

non-lifting bodies representing the nacelle and spinner have been added to establish their effect on the wake and interaction noise.

Another method of reducing the interaction noise is controlling the strength of the tip vortex. Various tip geometry parameters will be examined: sweep, dihedral, and twist. Tip sweep is used on modern turboprop aircraft to minimize transonic effects, but could also affect the formation of the tip vortex. Dihedral could be made to function similarly to winglets and reduce the magnitude of the vortex rolling off the tip through the same mechanism. Twist will directly impact the magnitude of the tip vortex by changing the loading distribution across the blade. Parametric studies have been conducted on these geometric features to establish their effect on the tip vortex and overall propeller noise.

Finally, off-design conditions were considered as these drastically change the flow around the propeller-wing configuration and the formation of the propeller's wake. Low speed and high angle of attack conditions were examined, representing takeoff and landing.

1.6. Thesis Overview

The present chapter introduced the research to be conducted in the context of turboprop noise reduction. The mechanisms by which propellers and wing interaction effects generate noise are introduced along with the methods used to predict their magnitude. Finally, the attempts by academia and industry to mitigate propeller noise are given followed by the motivation and objectives of the current work.

Chapter 2 outlines the methodology used to conduct the present research. The simulation software and environment is described along with the modifications made to the SmartRotor code to accommodate research into turbopropellers. The aerodynamic and aeroacoustic theory used by the code is described. Validation cases for each module are presented for the context of turbopropellers.

The third chapter presents the results of the tip shape parametric studies. Aerodynamic and acoustic performance of each of the modified blades is compared to the baseline blade. Trends in tip vortex strength, overall sound pressure level (OASPL), and 1st harmonic sound pressure level are identified.

Chapter 4 discusses the impact of the wing on the noise of a traditional tractor configuration. Results from a parametric study on relative wing placement are presented with noise data from each position. The local leading edge sweep of the wing is varied to attempt to minimize interaction noise. A complete propeller-nacelle-wing configuration is also examined and the aerodynamic and acoustic results presented.

Chapter 5 examines off-design conditions and their effect on noise. The high-angle of attack and low-speed conditions are examined both with and without the wing present in the propeller's wake.

The final chapter, Chapter 6, contains a final summary, concluding remarks, and recommendations for future work in this area.

2. Simulation Methodology

2.1. Research Methodology

The field of research in aeroacoustics, and propeller noise in particular, is conspicuously smaller than related aerodynamic fields. This is due in part to the inherent difficulty in aeroacoustic experimentation in wind tunnels. In order to conduct aeroacoustic measurements in a laboratory environment, specialized wind tunnel facilities that feature an open-jet anechoic test chamber are required. When testing propellers, it is also necessary to have a nearly silent drive system to be able to capture solely that noise created by the propeller. These stringent requirements drastically increase the cost of the facility and reduce their availability. For this reason, the present work makes sole use of computational tools.

The code used for this research, SmartRotor, was developed at Carleton University, combining an aerodynamic module created by the National Technical University of Athens (NTUA), a beam structural model coded at the Massachusetts Institute of Technology (MIT), and an aeroacoustic module developed at Carleton University. This code has previously been used for research into rotorcraft aeroacoustics and aerostructural investigation of active control for rotorcraft blades [40]–[43]. It has been extensively validated for rotorcraft applications through those projects.

In applying SmartRotor to turbopropeller applications, certain modifications had to be made to the code. This chapter will outline those modifications made, as well as the theory behind the aerodynamic and aeroacoustic modules. As the present work

treats all propellers as rigid bodies, the aeroelastic module has been disabled. Validation studies using experiments found in literature have been made for both the aerodynamic module and acoustic results and will also be presented in this chapter. Finally, the chapter will conclude with a summary of the capabilities and limitations of the SmartRotor code as it applies to turbopropellers.

2.2. Test Cases

The amount of literature on aeroacoustic experiments reflects the near-prohibitive nature of aeroacoustic experimentation. In fact, no suitable experiments could be found with both aerodynamic performance and noise data published. Instead, it was necessary to first validate the aerodynamic component of the code using an experiment with published thrust and torque values. While this is meager data on which to base an aerodynamic validation, it is the best that can be done with what literature exists. After the code was validated aerodynamically, the simulation parameters were changed to match those used in a test case for which acoustic data was published. As the field of propeller aeroacoustics is very narrow, only a single experiment exists in publicly-available literature containing the acoustic spectral results of a propeller in isolation [14]. The geometric parameters used for this second test case are similar to both the first test case and the baseline case that will be used in later chapters. Note that the consistency parameter used in propeller and rotorcraft aeroacoustics is tip speed as opposed to Reynolds or Mach number. This is why, despite having different forward and rotational speeds, the aerodynamic and aeroacoustic validation cases complement each other due to the fact that their helical tip speeds – that is, the vector

magnitude of the speed at which the propeller’s tip travels both forward and rotationally – are very similar. Note, however, that the increased rotational speed of the scaled propeller used means that the frequency spectra output will be scaled proportionally along the frequency axis compared to the full-size propeller.

Table 1. Validation Test Matrix.

Test Case	Case A	Case B	Case C
Reference	[9], [44]	[14]	
Blade Profile	NASA SR-2	NASA SR-2	NASA SR-2
Number of Blades	8	4	4
Diameter	0.622 m	0.591 m	0.622 m
Helical Tip Speed	294 m/s	261 m/s	294 m/s
Root Pitch Angle	60 degrees	21 degrees	60 degrees
Rotational Speed	6487 RPM	8200 RPM	6487 RPM
Axial Speed	204 m/s	62 m/s	204 m/s
Purpose	Aerodynamic Validation	Aeroacoustic Validation	Parametric Study Baseline

The NASA SR-2 propeller was used for this study as it is a straight blade designed for wind tunnel testing of turbopropeller blades [9] and a blade from it is shown in detail in Figure 3. Its geometry curves and an illustration of the 8-bladed propeller can be seen in Figure 4 and Figure 5, respectively.

Planform View

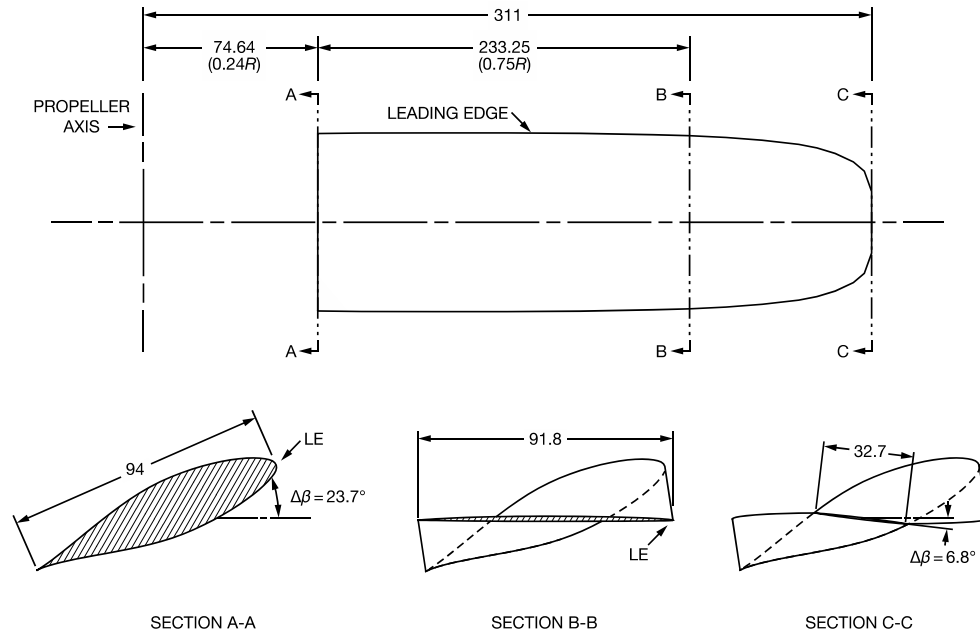


Figure 3. Technical drawing of the NASA SR-2 propeller.

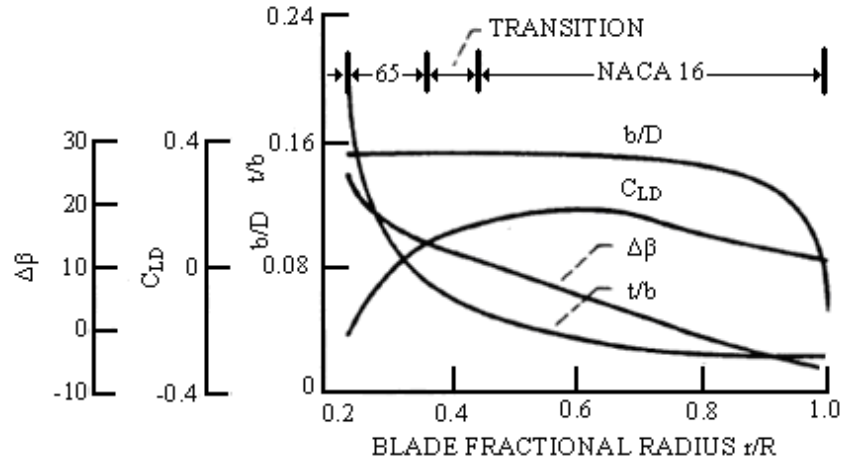


Figure 4. Propeller geometry curves of the SR-2 propeller used for the test case [44]. b/D is local chord non-dimensionalized by diameter, C_{LD} is the design lift coefficient for that station's airfoil, $\Delta\beta$ is the twist angle, and t/b is local relative thickness (thickness divided by chord).

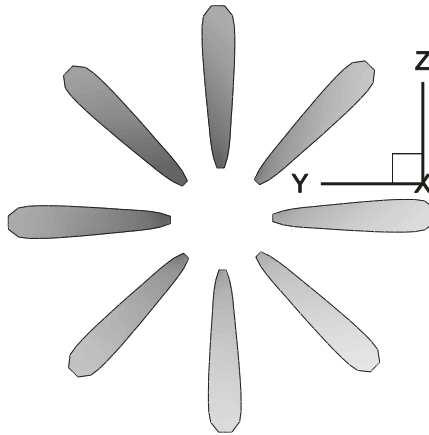


Figure 5. SR-2 geometry and axis convention.

2.3. Numerical Method

2.3.1. SmartRotor Aerodynamic Component

While predicting the aerodynamic performance of simple propellers in constant axial flow is relatively simple, the problem becomes vastly more complex when one wishes to examine the vortices and wakes generated by the propeller disk. Furthermore, the interaction between the rotating wake and stationary bodies makes predicting the flow even more difficult. Computational modeling of this environment requires accurately capturing the mutual interaction between all of the bodies and their wakes. Due to the time-varying aspect of the interaction between the rotating bodies and the stationary ones, and the inherent difficulty in resolving their wakes, this becomes a computationally expensive and challenging task.

Despite the challenges, accurate computational modeling forms the foundation of many related analyses. Aeroelastic and aeroacoustic analyses depend first and foremost on accurate aerodynamic input. To have any hope of accurately predicting

propeller or wing vortex interaction noise, it is first essential to accurately predict the aerodynamics of the system.

Typical computational fluid dynamics (CFD) software has been developed to the point where it can provide accurate predictions of the flow field with consistent success. While it is tempting to use CFD to model the propeller-wing system, certain drawbacks make its use impractical for this purpose. The grid-based nature of most CFD codes suffers from numerical dissipation that makes it very difficult to accurately capture wake effects. The wake predicted by these codes typically degrades much more quickly than seen in reality. Mitigating this by using an ultrafine mesh drastically increases the computational cost to the point of infeasibility. The time-varying aspect of the interaction between the rotating bodies and the stationary ones further complicates the task by requiring a transient simulation. This also increases the computational cost and difficulty of modeling.

Instead, an alternative method of CFD is used here: a coupled panel method and vortex free wake model. While the resolution of the flow field is significantly reduced, the loading on the bodies is calculated with reduced computational cost by several orders of magnitude. The SmartRotor code, developed at Carleton University, uses as its core aerodynamic component the GENERAL Unsteady Vortex Particle (GENUVP) code, which was originally developed at the National Technical University of Athens (NTUA) by Voutsinas et al. [45]. GENUVP uses a panel method for simulating the wake around the solid bodies and a coupled vortex wake method for predicting their wake. While the

initial use of GENUVP was for studying horizontal axis wind turbines, it has been extended to rotorcraft and, in the present work, to propellers. In the form of SmartRotor, the code has been extended to include an aeroelastic module and an aeroacoustic solver. For the purposes of the present work, the aeroelastic module has been disabled and the propellers treated as rigid bodies. The aeroacoustic component is described in Section 2.3.2. While the details of the GENUVP aerodynamic code are detailed in references [40], [45]–[47], the main aspects of its formulation are presented below.

As mentioned previously, GENUVP uses a coupled panel method and vortex particle method. This is an application of the Helmholtz decomposition, or vorticity transport theorem. Through the Helmholtz decomposition, the flow field can be separated into an irrotational component, due to the influence of the solid bodies on the flow, and a rotational component, due to the wakes emitted by the lifting bodies. Let $\vec{u}(\vec{x}, t)$, $\vec{x} \in D$, $t \geq 0$ represent the velocity field as a function of position, \vec{x} , and time, t , where D represents the domain. The velocity field is then decomposed according to the Helmholtz decomposition as follows:

$$\vec{u}(\vec{x}, t) = \vec{u}_{\text{ext}}(\vec{x}, t) + \vec{u}_{\text{solid}}(\vec{x}, t) + \vec{u}_{\text{near wake}}(\vec{x}, t) + \vec{u}_{\text{far wake}}(\vec{x}, t) \quad (2.1)$$

where \vec{u}_{solid} represents the velocity field generated as a consequence of the solid bodies representing wings, propeller blades, or engine nacelles. \vec{u}_{ext} represents any external velocity field from the movement of the reference frame. $\vec{u}_{\text{near wake}}$ and $\vec{u}_{\text{far wake}}$ are the velocity fields due to the near and far wakes, respectively. A panel method can be used to calculate \vec{u}_{solid} and $\vec{u}_{\text{near wake}}$ through the use of singularity

distributions over the surfaces of the bodies. $\vec{u}_{far\ wake}$ is obtained by the Biot-Savart law as shown in eq. (2.2). This equation can be evaluated using vortex methods that describe the vorticity of the flow field.

$$\vec{u}_{far\ wake}(\vec{x}, t) = \int_{D_{\omega}(t)} \vec{\omega}(\vec{x}_0, t) \times \frac{(\vec{x} - \vec{x}_0)}{4\pi|\vec{x} - \vec{x}_0|^3} dD \quad (2.2)$$

Together with, and coupled appropriately with, the panel method, this can be used to evaluate eq. (2.1) to describe the flow field.

2.3.1.1. Panel Method

The panel method implemented in SmartRotor for calculating the effect of solid bodies on the flow field is based on the work by Hess [48], [49]. This method assumes an incompressible and inviscid potential flow. The continuity equation can therefore be reduced to the Laplace equation:

$$\nabla^2 \phi = 0 \quad (2.3)$$

where ϕ is the scalar velocity potential. Two conditions are applied to the velocity potential solution: that it not penetrate any solid boundaries, and that the flow be regular.

$$\nabla \phi \cdot \vec{n}|_S = \frac{\partial \phi}{\partial n}|_S = (\vec{u}_{ext} \cdot \vec{n} - F)_S \quad (2.4)$$

$$|\nabla \phi|_{\infty} \rightarrow 0 \quad (2.5)$$

where S is the surface of any given body, \vec{n} is the local outward normal unit vector of said surface, and F is the local normal velocity due to the motion of the body and far-wake induced velocity.

General solutions to (2.3) may be constructed using Green's identity in terms of source and dipole distributions over the surfaces of the bodies in the flow field. For non-lifting bodies, such as the engine nacelle or spinner, the velocity potential due to the body is found by defining a continuous source distribution over its surface. The potential induced at a given point, \vec{P} , is found by integrating the local source intensity, σ , over the surface by eq. (2.6).

$$\phi(\vec{P}) = \int_S \sigma \left(\frac{1}{r} \right) dS \quad (2.6)$$

For lifting bodies, such as propeller blades or the aircraft's wing, a dipole distribution is necessary to create circulation around the body to generate a net lifting force. For thick airfoils, both a source and dipole distribution are used to model the surface as well as the lifting effect. Dipole sheets are also trailed downstream of the body to form near-wake surfaces to satisfy the condition of conservation of circulation needed by Kelvin's theorem. For lifting bodies, the potential induced at a given point due to the local dipole intensity, μ , is found by integrating over the lifting body or wake surface by eq. (2.7).

$$\phi(\vec{P}) = \int_S \mu \sigma \cdot \nabla \left(\frac{1}{r} \right) dS \quad (2.7)$$

$$\phi(\vec{P}) = -\frac{1}{4\pi} \left(\int_{\text{Lifting}} \mu \vec{n} \cdot \nabla \left(\frac{1}{r} \right) dS + \int_{\text{Non-lifting}} \sigma \left(\frac{1}{r} \right) dS + \int_{\text{Wake}} \mu \vec{n} \cdot \nabla \left(\frac{1}{r} \right) dS \right) \quad (2.8)$$

The velocity potential, then, is the sum of all these distributions, resulting in eq. (2.8). Since eqs. (2.6) and (2.7), and therefor (2.8), all meet the condition of regularity, the condition of non-penetration of the surface (eq. (2.4)) must be combined with eq. (2.8) to satisfy all the conditions imposed.

$$-\frac{1}{4\pi} \left(\int_{\text{Lifting}} \mu \nabla \left(\frac{\partial}{\partial n} \frac{1}{r} \right) dS + \int_{\text{Non-lifting}} \sigma \nabla \left(\frac{1}{r} \right) dS + \int_{\text{Wake}} \mu \nabla \left(\frac{\partial}{\partial n} \frac{1}{r} \right) dS \right) \cdot \vec{n} = \vec{u}_{\text{ext}} \cdot \vec{n} - F \quad (2.9)$$

This equation is then evaluated over all surfaces and defines the governing equation for the panel method used in SmartRotor.

In SmartRotor, the surfaces of the bodies and near-wakes are discretized into panel elements so that eq. (2.9) can be approximated by a system of linear equations. A single strip of near-wake elements is retained for each time step and transformed into wake particles in the far wake before the proceeding time step.

Figure 6 shows an example of a complete propeller, spinner, nacelle, and wing configuration mesh that shows the discretization of each body. Since each panel's source and/or dipole (depending on the type of body) intensity is constant over the area of the panel, the source and dipole intensities can be extracted from the integrals in eq. (2.9). As the remaining integrals rely simply on the geometry and discretization, they result in constant matrices of influence coefficients, C , when evaluated at the control points of each panel element.

$$[C^{\text{Lifting}}_{ij}]\{u_j\} + [C^{\text{Near wake}}_{ik}]\{u_k\} + [C^{\text{Non-lifting}}_{il}]\{\sigma_l\} = \{\vec{u}_{\text{ext}} \cdot \vec{n} - F_i\} \quad (2.10)$$

$i = 1, (N_{\text{Lifting}} + N_{\text{Non-lifting}}) \quad j = 1, N_{\text{Lifting}} \quad l = 1, N_{\text{Non-lifting}} \quad k = 1, N_{\text{Near wake}}$

The resulting equation, (2.10), is the linear system approximation of eq. (2.9), where N_{Lifting} , $N_{\text{Non-lifting}}$, and $N_{\text{Near wake}}$ represent the panels on each lifting, non-lifting, and near-wake surface respectively.

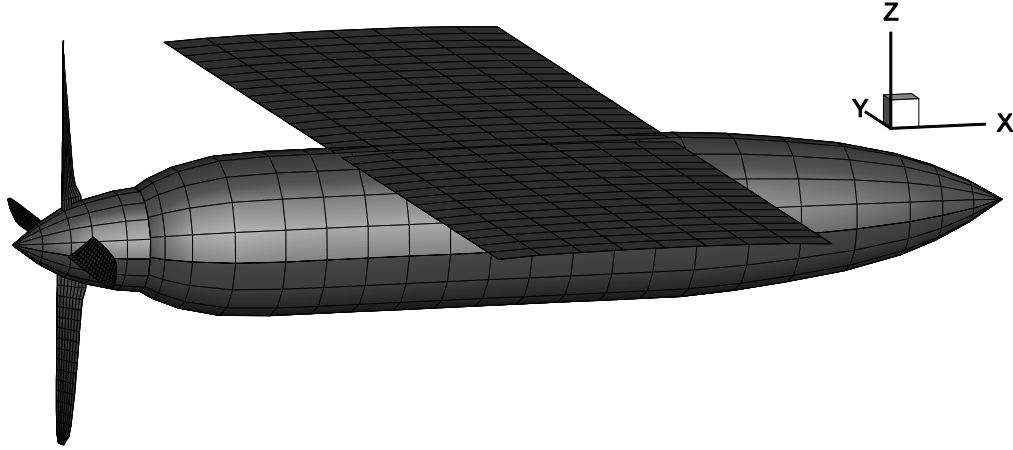


Figure 6. Example surface discretization.

A unique solution to the system requires applying certain physical conditions on the near-wake [50]. The dipole intensities of each near-wake element is set to equal the value of the adjacent emitting elements on the lifting body along the trailing edge and tip. This enforces a zero pressure jump Kutta condition. The geometry of the near wake is determined from the flow velocity at the edges from which it is emitted.

Equation (2.10) is then solved for the necessary source and dipole distributions. From this, a discretized form of eq. (2.8) can be used to determine the scalar velocity potential at any given point in the flow field. The velocity field can, in turn, be calculated from the potential using eq. (2.1), knowing eq. (2.11), below.

$$\vec{u}_{\text{panel}} = \vec{u}_{\text{solid}} + \vec{u}_{\text{near wake}} = \nabla\phi \quad (2.11)$$

The pressure distribution and potential loads on the solid bodies can be calculated from the unsteady Bernoulli equation (eq. (2.12)). On thin lifting bodies, SmartRotor also corrects the potential load distribution to account for the leading edge suction force [42], [51].

$$C_p = 1 - \frac{u^2}{u_{\text{ref}}^2} - \frac{2}{u_{\text{ref}}^2} \frac{\partial\phi}{\partial t} \quad (2.12)$$

2.3.1.2. Vortex Particle Method

The vortex particle method used by SmartRotor is a free wake vortex particle method. This is as opposed to a fixed wake model where the geometry of the wake is pre-specified based on *a priori* analytical or experimental information. Free wake methods develop the shape of the wake as the simulation progresses using numerical integration of vorticity transport equations. While these are much more computationally expensive than fixed wake methods due to the need to track the wake structure and the huge number of calculations required to capture the self-interacting nature of the wake, free wake methods offer much greater accuracy by actually determining the structure of the wake by simulation than whichever approximation is given to the model.

The vortex particle method treats the wake as a cloud of vortex particles, each with vector quantities of position, velocity, and intensity. The Biot-Savart law is applied using the intensity of each vortex particle to determine the effect on the surrounding velocity field. From eq. (2.2), D_ω is decomposed into volume elements with a vortex

particle assigned to each one. Now let $\vec{\Omega}_j(t)$ and $\vec{Z}_j(t)$ denote the vorticity and position, respectively, of a given vortex particle, j . Vorticity is defined as:

$$\vec{\Omega}_j(t) = \int_{D_{\omega,j}} \vec{\omega}(\vec{x}, t) dD \quad (2.13)$$

such that

$$\vec{\omega}(\vec{x}, t) = \sum_j \vec{\Omega}_j(t) \delta(\vec{x} - \vec{Z}_j(t)) \quad (2.14)$$

$$\vec{\Omega}_j(t) \times \vec{Z}_j(t) = \int_{D_{\omega,j}} \vec{\omega}(\vec{x}, t) \times \vec{x} dD \quad (2.15)$$

The far-wake induced velocity then can be expressed as shown in eq. (2.16). Note, however that this equation is highly singular and so a smooth approximation, developed by Beale and Majda [52], is used, resulting in eq. (2.17).

$$\vec{u}_{\text{Far wake}}(\vec{x}, t) = \sum_j \frac{\vec{\Omega}_j(t) \times (\vec{x} - \vec{Z}_j(t))}{4\pi |\vec{x} - \vec{Z}_j(t)|^3} \quad (2.16)$$

$$\begin{aligned} \vec{u}_{\text{Far wake}}(\vec{x}, t) &= \sum_j \frac{\vec{\Omega}_j(t) \times \vec{R}_j}{4\pi R_j^3} f_\varepsilon(R_j) \\ \vec{R}_j &= \vec{x} - \vec{Z}_j(t) \\ f_\varepsilon(R_j) &= 1 - e^{-(R_j/\varepsilon)^3} \end{aligned} \quad (2.17)$$

In this equation, ε is the cut-off length for the vortex particles. This changes the method used from a vortex particle method to a vortex ‘blob’ method. Vortex blob methods have been proven to be automatically adaptive, stable, convergent, and of arbitrarily high-order accuracy. SmartRotor, for example, uses a second order space and

time discretization. The vortex ‘blobs’ are then convected in a Lagrangian sense, using eqs. (2.18) and (2.19), where \vec{D} is the deformation tensor.

$$\frac{d\vec{Z}_j}{dt} = \vec{u}(\vec{Z}_j, t) \quad (2.18)$$

$$\frac{d\vec{\Omega}_j}{dt} = (\vec{\Omega}_j \nabla) \vec{u}(\vec{Z}_j, t) = \vec{D} \cdot \vec{\Omega}_j \quad (2.19)$$

To develop the far wake from the near wake, some simple coupling conditions are applied. The panel method calculations are performed for a given time step, following which the near wake strip panel elements are transformed into vortex particles whereupon they become part of the far wake. The vorticity of each near wake dipole element is integrated over its surface and formed into a vortex particle at the control point. This new vortex particle becomes part of the far wake and is convected as the far wake propagates prior to the beginning of the subsequent time step. This process is shown in Figure 7.

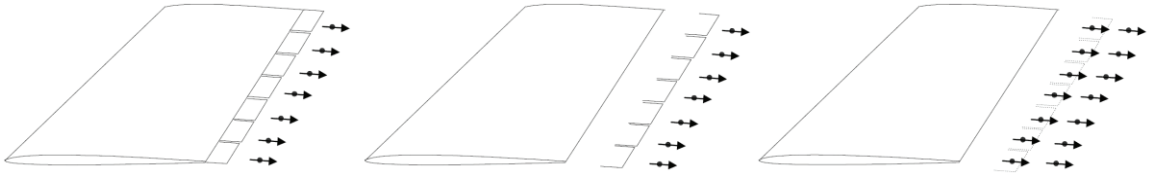


Figure 7. The formation of vortex particles from a trailing edge wake strip [40].

2.3.2. SmartRotor Aeroacoustic Component

Given that analytical approaches such as those by Gutin and Deming mentioned earlier are incompatible with the complexities induced by the presence of a wake, it is necessary to turn to computational aeroacoustics (CAA). There are two base methods upon which other specific solutions or formulations are based: the Lighthill acoustic

analogy, which rearranges the Navier-Stokes equation into a wave form; and the Kirchhoff integral, which begins with the wave equation and is then applied to fluid dynamics. The acoustic analogy is the one most commonly used because it contains all aeroacoustic sources and was found to be superior because of it strictly following the governing equations [53].

At the core of the aeroacoustic module of SmartRotor is the Ffowcs-Williams Hawkins equation [42]. The FW-H equation, which is based on the Lighthill acoustic analogy, approaches the problem of aerodynamically-generated sound from a body in arbitrary motion in a fluid. It does this by treating the problem as one of mass and momentum conservation, with a mathematical discontinuity representing the surface of the body. Within the surface, the flow is arbitrary, although usually asserted to be at rest, while on the exterior the flow is the same as the physical exterior flow. The surface discontinuity is created using mass and momentum sources, which also act as sound generators. These sources are approached according to the acoustic analogy by combining the mass and momentum conservation equations and rearranging them to obtain a wave equation.

The FW-H equation describes the acoustic pressure, p' , at the observer position, \vec{x} , generated by a body moving through fluid. Let \vec{x} and \vec{y} be the observer and source position vectors, respectively, and let $f(\vec{v}, t) = 0$ describe the motion of the surface of the body ($f > 0$ outside the body). The FW-H equation is then as follows:

$$\left(\frac{1}{c^2} \frac{\partial^2}{\partial t^2} - \nabla^2\right) p' = \frac{\partial}{\partial t} [\rho_0 v_n |\nabla f| \delta(f)] - \frac{\partial}{\partial x_i} [l_i |\nabla f| \delta(f)] + \frac{\partial^2}{\partial x \partial y} [T_{ij} H(f)] \quad (2.20)$$

where c and ρ_0 are, respectively, the speed of sound and the density of the undisturbed medium, $v_n = v_i n_i$ is the local normal velocity on the surface, l_i is the local force on the fluid per unit area, and T_{ij} is the Lighthill stress tensor, which accounts for viscous effects. Note that $\delta(f)$ and $H(f)$ are the Dirac delta and Heaviside functions, respectively. The right hand side of the equation can be broken down into its three component parts, describing the thickness, loading, and quadrupole noise sources, in that order.

Thickness noise accounts for the noise generated due to the displacement of the fluid by the finite thickness of the body. As the body moves through the fluid, the fluid moves out of its way and then back in behind it. This motion generates an acoustic pressure pulse. Loading noise accounts for the noise generated due to the loading and changes of loading on the body. Changes in loading or movement of a loaded body translates to changes to the local acoustic pressure. Quadrupole noise is generated by shear forces and compressibility effects. Quadrupole noise is a volume source while thickness and loading are surface sources. Figure 8 shows the physical meaning of these noise sources.

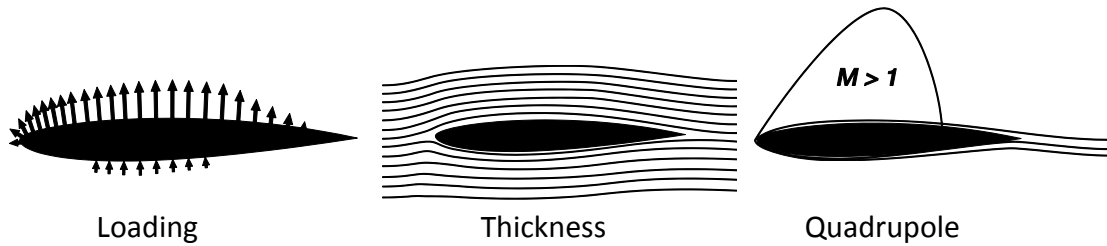


Figure 8. Physical meaning of the sources seen in the FW-H equation, based on [42].

The aeroacoustic module in SmartRotor neglects quadrupole noise sources because accounting for them would require a grid-based solver to simulate the flow within the volume. However, as thickness and loading noise accounts for the majority of the acoustic pressure when the flow is not in the high-transonic regime, neglecting the quadrupole term is a practical approximation [54] as it is insignificant for subsonic flows and may be neglected [53]. So while the harmonic noise of propeller blades will be slightly underpredicted in cases of high tip speed (by up to 3 dB [44], [54]), the noise prediction using only thickness and loading sources is valid in most cases.

SmartRotor implements Farassat's 1A solution of the FW-H equation. The 1A formulation has been used extensively in the field of computational aeroacoustics (CAA) and has been thoroughly validated. Most CAA codes use Farassat's 1A formulation or derivatives thereof, for example, to approximate the quadrupole term. The 1A formulation is a solution to the thickness and loading terms of the FW-H equation by integrating over the body's surface. The three equations below show the equations for the loading and thickness acoustic pressures followed by the total acoustic pressure, found via superposition, respectively, for the observer position, \vec{x} .

$$4\pi p'_{\text{Loading}}(\vec{x}, t) = \frac{1}{c} \int_{f=0} \left[\frac{\dot{l}_i \vec{r}_i}{r(1-M_r)^2} \right]_{ret} dS + \int_{f=0} \left[\frac{l_r - l_i M_i}{r^2(1-M_r)^2} \right]_{ret} dS \quad (2.21)$$

$$+ \frac{1}{c} \int_{f=0} \left[\frac{l_r(r\dot{M}_i \vec{r}_i + cM_r - cM_i^2)}{r^2(1-M_r)^3} \right]_{ret} dS$$

$$4\pi p'_{\text{Thickness}}(\vec{x}, t) = \int_{f=0} \left[\frac{\rho_0 v_n (r\dot{M}_i \vec{r}_i + cM_r - cM_i^2)}{r^2(1-M_r)^3} \right]_{ret} dS \quad (2.22)$$

$$p'(\vec{x}, t) = p'_{\text{Loading}}(\vec{x}, t) + p'_{\text{Thickness}}(\vec{x}, t) \quad (2.23)$$

where $\vec{r} = \vec{x} - \vec{y}$, $M_i = v/c$, $M_r = M_i r_i/r$, and $l_r = l_i r_i/r$. The $[]_{ret}$ subscripts indicate those integrals that are evaluated in the source time frame, τ , that is, the time that the acoustic pressure signal is emitted. The acoustic signal is received at the observer position in the observer time frame, t . Similarly to the aerodynamic equations, the integrals found here are approximated by discretizing the body surface and calculating the contributions of each element.

The aeroacoustic component of SmartRotor uses the same geometric and temporal discretization as the aerodynamic component. Each panel from the potential model acts as an acoustic source. The aeroacoustic module executes after the potential calculations, from which the aerodynamic loading results are used to calculate the emitted acoustic signal. The loading noise contributions for a given panel are calculated as a function of loading, panel velocity, and relative position from the observer. Viscous corrections are not implemented in SmartRotor's acoustic module. The total acoustic pressure at each virtual microphone is determined by the summation of the contributions of each panel, accounting for the different travel times of each acoustic signal.

The time sequencing for acoustic signals transforms each emission from the source time frame, τ , to the observer time frame, t . For a given acoustic signal, an approximation of the relationship between these two frames is as follows:

$$t = \tau + \frac{|\vec{r}|}{c + \vec{u}_\infty \cdot \vec{r}} \quad (2.24)$$

This equation accounts for the speed of sound travel time delay from the point of emission to the observer. The acoustic pressure at the observer, in the observer time frame, is updated with this contribution. While both time frames are discretized using the same discretization as the aerodynamic component, it is generally not the case that an acoustic signal arrives exactly at the endpoint of a time step in the observer time frame. Linear interpolation is used to distribute the contribution of the signal between the two time steps that bound the arrival of the acoustic signal.

Special treatment is applied to the calculation of thickness noise for thin lifting bodies. The thickness noise term is dependent on the flow velocity normal to the surface of the physical body as opposed to the thin approximation thereof. To account for this, virtual upper and lower surfaces are created using known airfoil geometry. The normal velocity is then calculated using the velocity of the mean surface panel and the normal vectors of the virtual panels.

The resulting acoustic pressure time history is then passed through a Fast Fourier Transform to convert it from the time domain to the frequency domain in which sound is studied, in this case using the MATLAB `fft` function. The documentation for this command can be found in reference [55]. In addition to the frequency spectrum, sound

levels can also be expressed in terms of the Overall Sound Pressure Level (OASPL). This value is calculated using eq. (2.25), below. As the time history is uniformly discrete, the approximation on the right is used. Note that p'_{ref} is the acoustic reference pressure, for which 20 μ Pa is commonly used [5].

$$OASPL = 20 \log_{10} \frac{\sqrt{\frac{1}{t_2 - t_1} \int_{t_1}^{t_2} p'(t)^2 dt}}{p'_{ref}} \cong 20 \log_{10} \frac{\sqrt{\frac{1}{n} \sum p_t'^2}}{p'_{ref}} \quad (2.25)$$

2.3.3. Modifications to the SmartRotor Code

Given the large number of simulations to be run for the wide range of parametric studies conducted for this research, computational speed was of paramount importance. Using the original code, last developed in 2011, a test case of the 8-bladed SR-2 propeller took six days to run approximately six rotations at 180 time steps per rotation. This rate would have made parametric studies infeasible. The existing attempt at parallelization was removed, replaced, and augmented in subroutines previously run in serial, leading to a speed increase of an order of magnitude. Minor code optimizations were also made by restructuring certain loops and making use of features added to the Fortran language since Fortran77.

One of those features, dynamic memory allocation, also permitted the removal of hard-coded limitations for the number of time steps, blades, elements, and other important parameters. Now, the length of simulations or the number of bodies simulated is limited only by hardware and the operating system as opposed to a hard,

arbitrarily imposed cap within the code. This also reduced the memory consumed by the software for shorter or less complex simulations, aiding computation time and freeing up system resources for other tasks.

Two important modifications were made to the functionality of the code in order to accommodate propellers that were previously unnecessary when studying rotorcraft using the SmartRotor code. Helicopter blades are typically a constant airfoil across the span, or at least can be approximated as such. Because of their higher rotation speed and shorter span, the airfoil distribution of a propeller is much more complex. It was necessary to modify the geometry initialization subroutine, the aerodynamic module, and the aeroacoustic module to not only handle spanwise variations in airfoil, but also generic airfoils.

Some work on the aerodynamic module was previously completed to use trilinear interpolation to account for spanwise airfoil distributions in the airfoil performance lookup subroutine. This work was re-implemented and made more robust.

The modifications made to the geometry and aeroacoustic modules involved creating new subroutines for defining the surface of arbitrary airfoils. The geometry initialization subroutine relies on this information for defining the camber line surface for thin airfoils while the aeroacoustic module needs the slope of the upper and lower surfaces as part of the calculation of thickness noise. Previously, the geometry subroutine could accommodate NACA 4- and 5-series airfoils and the aeroacoustic module was only able to generate NACA 4- and 65-series airfoils. To allow generic

airfoils and arbitrary spanwise distributions, the code reads in the spanwise airfoil distribution and a series of airfoil coordinate files. From these, it generates spline curves of the 2-D airfoils and interpolates along the chord and span to generate the thin wing surface. The mean of the two surfaces is then taken to generate the camber line surface while the derivative in the chordwise direction is calculated and passed to the aeroacoustic module.

The aeroacoustic module, being previously limited to only two NACA thin wing airfoils, was also unable to calculate the impact on noise from non-lifting bodies or thick wings. The aeroacoustic module was extended to include the elements of a non-lifting body when calculating the contribution of each element to loading noise using eq. (2.21). Equation (2.22) was similarly enabled for non-lifting bodies. As opposed to thin bodies only one side of the surface is used, as there is no need to create a second virtual surface for the other side of the body due to the presence of closed three-dimensional geometry.

2.4. Verification

As the numerical method used is not grid-based, the typical definition of the computational domain is irrelevant. Vortex particles and bodies are tracked using their coordinates in three-dimensional space as opposed to grid cells. The panel method does, however, discretize bodies into panel elements over which pressures and velocities are calculated. The geometry curves (such as from Figure 4) are input to SmartRotor as lookup tables of radial position and the value. The code then generates

the geometry given these and the number of chordwise and spanwise panels. A uniform distribution was used both for chordwise and spanwise panels, as illustrated in Figure 9. The simulation is very sensitive to both relative element size and aspect ratio and will quickly diverge if the elements are not properly sized. For the present work, all propeller blades use 16 spanwise elements and 8 chordwise elements.

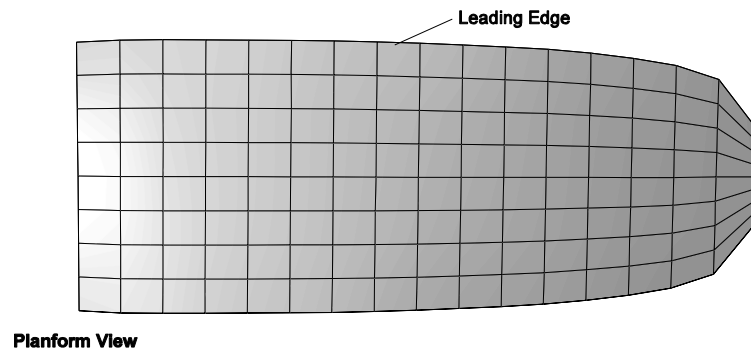


Figure 9. Mesh distribution on a blade.

Grid convergence results for the number of both spanwise and chordwise elements is shown below in Figure 10. The convergence variables used are the same as those that will be used as metrics throughout this work: first harmonic sound pressure level (1HSPL), and Overall Sound Pressure Level (OASPL). The acoustic variables are used because of their inherent sensitivity to aerodynamic performance – for the acoustic results to be converged, the aerodynamic results must first converge. The verification results presented here are for Case C, the parametric study baseline, from Table 1.

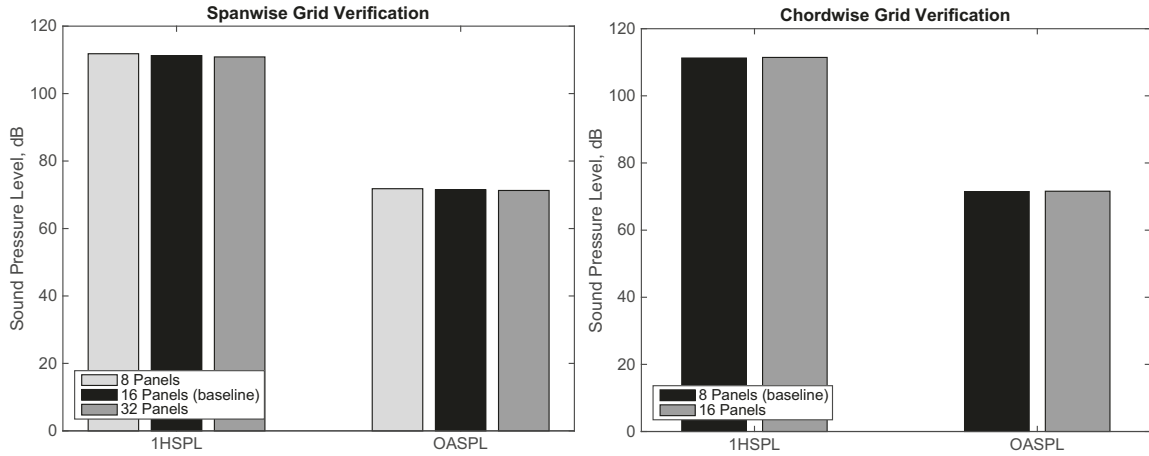


Figure 10. Grid convergence results for spanwise elements (left) and chordwise elements (right).

As many of the results deal with the frequency domain, it was also necessary to ensure that time convergence was also achieved. To do this requires ensuring a sufficient simulation length to resolve low frequencies as well as a small enough time step to resolve high frequencies. The time step also affects the bandwidth output from the Fourier transform. Figure 11 shows the effect of both time step size (presented as number of time steps per revolution) and simulation length (shown as number of revolutions).

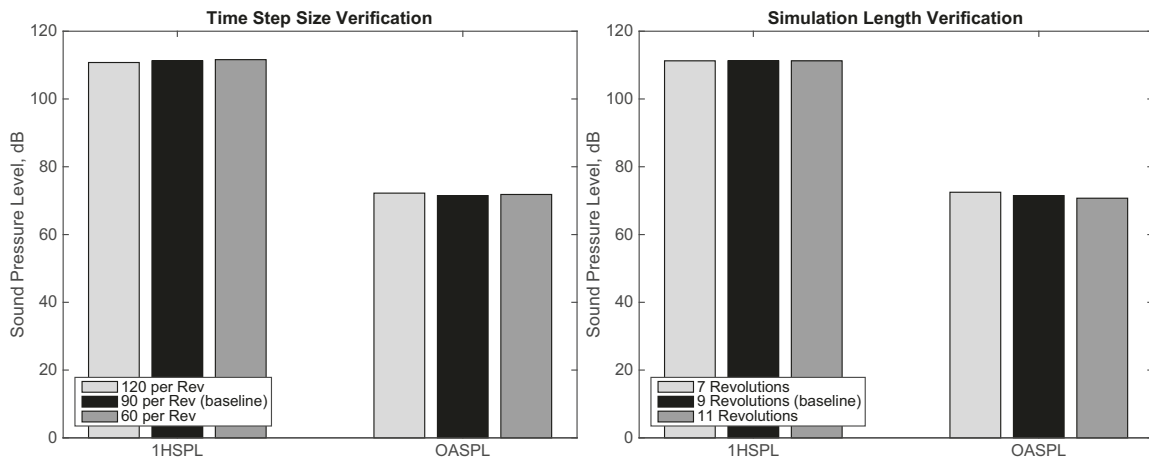


Figure 11. Time step size (left) and simulation length (right) convergence results.

To transform the acoustic pressure time histories into the frequency domain, MATLAB's `fft` function was used. The pressure time history was first truncated at the beginning and end to remove the effects of initial transience and wake activation at the start of the simulation and the effect of noise sources closer to the microphone expiring sooner (in the observer time frame) than those further away at the end of the simulation. A peak-to-peak window was then applied to the time history to minimize the effect of passing a finite series through the FFT. An example of the resulting acoustic pressure time history is shown in Figure 12 along with its resulting frequency spectrum in Figure 13. Because of the highly periodic nature of the resulting data and the large number of periods over which it extended, additional windowing functions had no effect on the resulting spectrum and were not used.

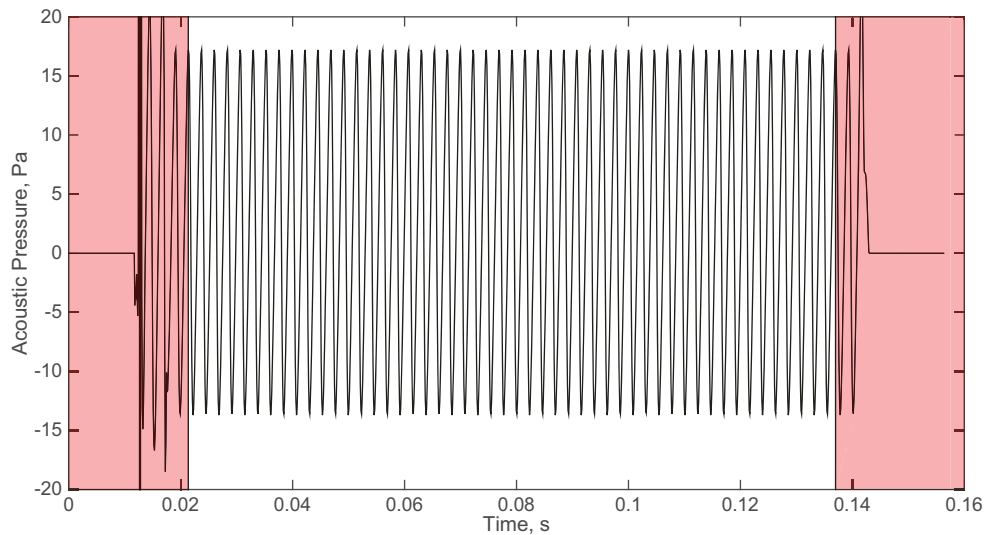


Figure 12. Example acoustic pressure time history with rejected regions highlighted.

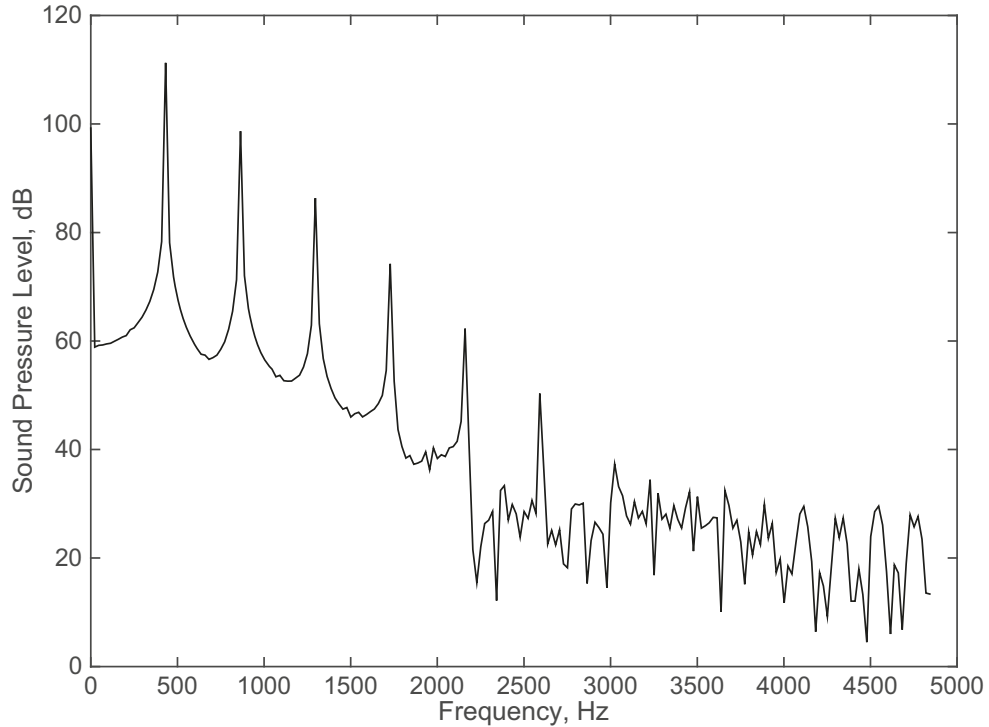


Figure 13. Resulting frequency spectrum from the example time history.

2.5. Aerodynamic Validation

While the SmartRotor code has been extensively validated for rotorcraft and horizontal-axis wind turbines [40], [41], [46], [50], it was necessary to validate it for propellers with high axial flow speeds and rotation speeds. This validation further served to validate the changes made to the code to handle spanwise varying airfoils. Aerodynamic performance data for the NASA SR-2 propeller is available from several sources [9], [44]. The test case used is that from De Gennaro et al. [44], with test parameters as outlined in Table 2. The flow conditions used represent one of two cruise condition design points of the SR-2. Because none of the available literature contained both high-quality aeroacoustic data and aerodynamic performance data for the same

set of conditions, the aerodynamic validation was conducted separately from the aeroacoustic validation.

Table 2. Aerodynamic validation test parameters.

Diameter	0.622m
Blade design	SR-2
Number of blades	8
Reference pitch	60
Rotational speed	6487 RPM
Axial speed	204m/s (Mach 0.6)

The primary characteristic to match when validating propeller aerodynamic performance is total thrust. While blade spanwise thrust loading would provide a more accurate metric, it is often unavailable due to the difficulty of instrumenting blades to measure thrust. Total thrust and torque are quite easy to measure in an experimental environment and are thus often the only data reported.

Table 3 shows the results from SmartRotor compared to the results provided by De Gennaro [44] and Dittmar [9]. It was necessary to increase the root pitch angle of the blades by 1 degree to match power coefficients. De Gennaro [44] also found this increase to be necessary and further simulations using a custom Blade Element Momentum Theory (BEMT) code [56] and the commercial CFD software StarCCM+ also reached the same conclusion. It is suspected that the original data by Dittmar [9] may have an error in the reported root pitch angle.

Table 3. Aerodynamic validation results.

Source	Dittmar	De Gennaro	SmartRotor	SmartRotor (without root pitch increase)
Power Coefficient	1.32	1.34	1.37	1.22

It is noted that the high axial flow rate convects the wake downstream much more quickly than, say, a helicopter in hover, and so the wake has less of an effect on the propeller. This reduces the number of revolutions required to reach periodicity. Figure 14 shows the highly periodic nature of the wake after only a few revolutions with the starting rollup from the impulsive start highlighted downstream.

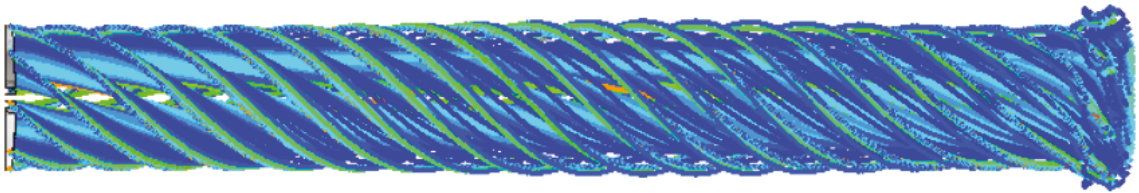


Figure 14. Wake visualization after three revolutions.

2.6. Aeroacoustic Validation

The modified acoustic module was validated for propellers in forward flight using a 4-bladed SR-2 propeller similar to that used in the aerodynamic validation. Acoustic data for turbopropellers is rare in literature. The only dataset found to contain frequency spectra [14] did not also contain aerodynamic results. This is why the aerodynamic and aeroacoustic validation was conducted in two parts. Table 4 summarizes the test setup for the aeroacoustic validation case.

Table 4. Aeroacoustic validation test setup.

Diameter	0.591m
Blade design	SR-2
Number of blades	4
Reference pitch	21
Rotational speed	8200 RPM
Axial speed	62 m/s (Mach 0.18)

While the results from SmartRotor matched those of the experiment well across a range of microphone locations, it was necessary to choose one location to be representative. This location was chosen to be at 90 degrees to the propeller axis (i.e. in the propeller disk plane) because that is the approximate angle at which the directivity of the propeller noise is at a maximum. Figure 15 shows a comparison of the frequency spectra calculated by the SmartRotor code compared to the experimental results at the chosen microphone location. The microphone is positioned 4.27m from the hub, which places it in the acoustic far field. Far field noise is the most repeatable measurement, which is why it is often reported in experimental results without accompanying near field data. The experiment by Soderman and Horne [14] includes one microphone in the acoustic near field, however the authors of the experiment admit skepticism of its reliability and so only their far field data is used in the validation.

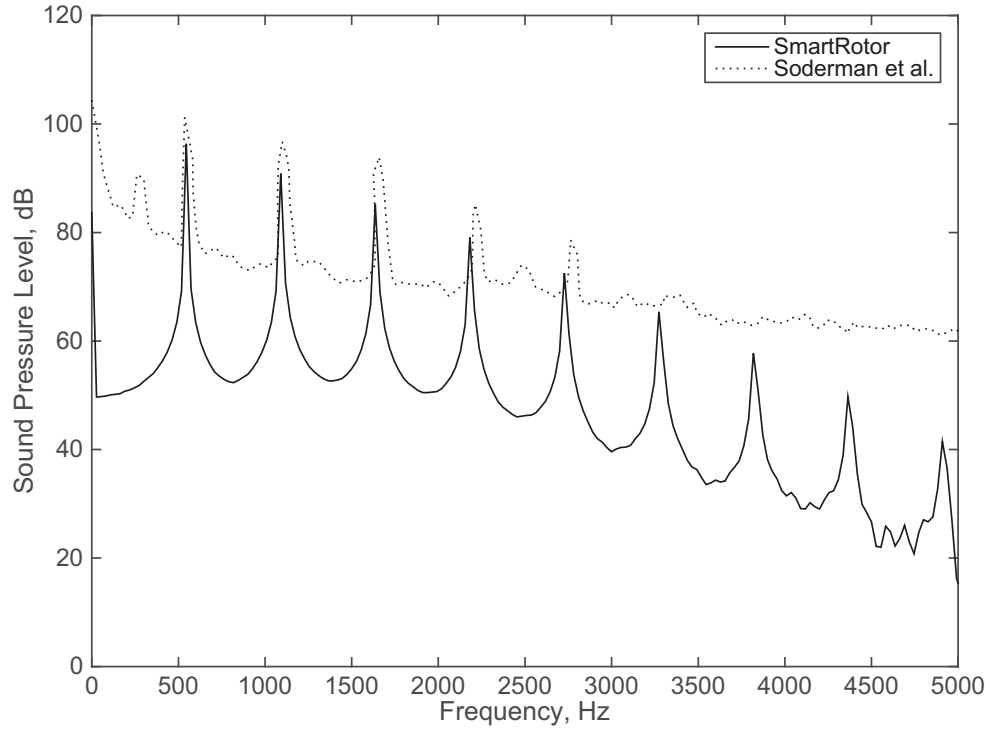


Figure 15. SmartRotor acoustic results.

The peaks match the experimental results almost exactly in both frequency and magnitude. The broadband noise component predicted by SmartRotor is lower than that recorded in experiment, however this is due to the clean acoustic computational environment provided by SmartRotor compared to the inherently noisy wind tunnel environment.

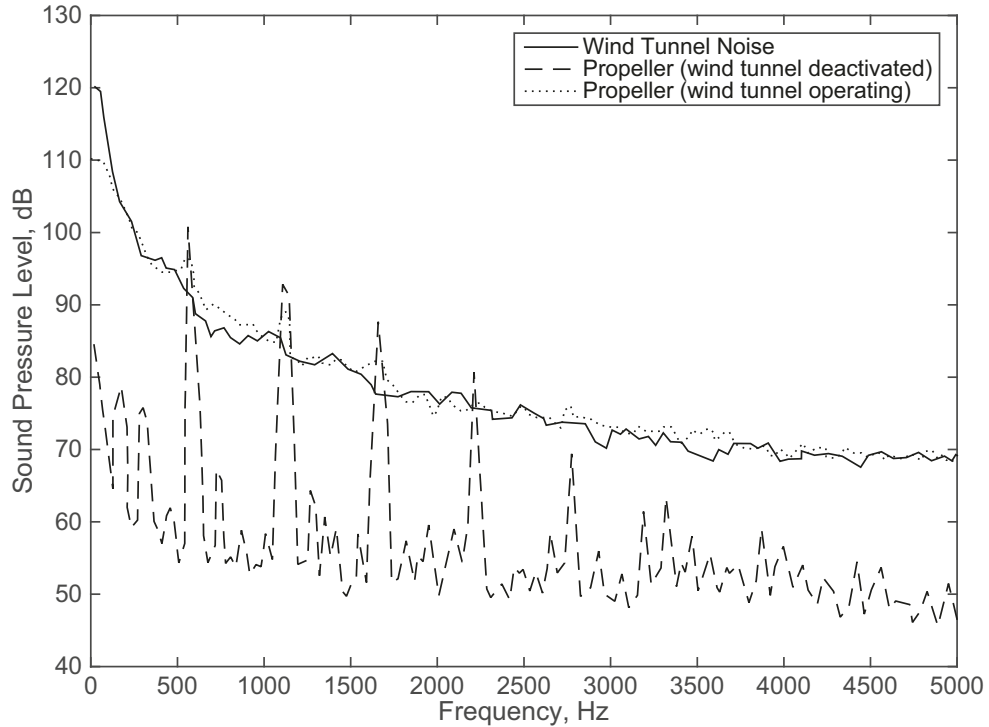


Figure 16. Acoustic spectra showing the effect of wind tunnel background noise.

Looking at the acoustic results for the experimental test case of an empty wind tunnel and their comparison of propeller noise with the wind tunnel operational or not, both shown in Figure 16, reinforces this theory. The discrepancy between SmartRotor and the experiment is not due to the neglected quadrupole noise sources as any shockwave noise sources would be travelling with the blade and would manifest as harmonic noise instead of broadband noise [57]. Attempting to account for wind tunnel noise by summing it with the computational results would bring the results into better agreement with the experiment, however there is no scientific value to be had in doing so.

In any case, harmonic noise, especially the first three harmonics, is the primary contributor to noise and is considered the most important to predict accurately.

Knowing that this is the case, and that broadband noise is at least reasonably well predicted allows the use of overall sound pressure level trends and harmonic noise data to be extracted from SmartRotor with a high level of confidence.

2.7. Summary of SmartRotor Capabilities and Limitations

The SmartRotor code is a computationally efficient method of predicting aerodynamic performance and noise of propellers, subject to certain limitations. First among these is that the incompressible nature of the panel and vortex particle methods requires that the flow be subsonic. Transonic tip speeds in excess of the critical Mach number of the specified airfoils may be used so long as the airfoil performance lookup tables include accurate performance data for those Mach numbers. At these speeds, however, the aeroacoustic module will begin to underpredict noise as quadrupole noise can no longer be neglected and the surface-based method cannot compute the volume-based noise source of Mach effects.

While generally requiring less computational time than other CFD codes, the efficiency of SmartRotor declines for simulations involving large numbers of wake-emitting bodies. As the computation time increases drastically with the number of wake particles, many-bladed propellers will become infeasible. Fortunately, these tend towards being classified as fans and so the code will be practical for our purposes.

Aside from these limitations, SmartRotor appears to be able to predict with good accuracy the noise and aerodynamics of systems of lifting and non-lifting bodies, taking

into account their mutual interactions and the effect of their wakes as they move relative to the fluid and each other.

3. Effect of Tip Shape on Vortex Structure

3.1. General Setup

Moving towards the goal of understanding the wing vortex interaction (WVI) noise, it was first necessary to examine further the propeller tip vortex structure. As mentioned earlier, it is believed that the tip vortex impinging on the wing is a significant source of noise both due to the fluctuating loading induced [18], [19], [24], but also due to the intersection of the vortex by the wing [58]. It is theorized in this research that the geometric characteristics of the propeller may be useful in managing the tip vortex strength and the way in which it propagates. In order to explore this concept, parametric studies on the effect of blade tip sweep, dihedral, and twist were conducted with the goal of determining the influence of geometric parameters and characteristics on tip vortex strength and noise. The primary objective was the investigation of tip vortex strength with the goal of applying this to studies on the interaction noise between the propeller tip vortex and an aircraft's wing. As any increase in propeller noise as a side effect of managing the tip vortex strength runs contrary to mitigating wing-vortex interaction (WVI) noise, the overall sound pressure level (OASPL) and first harmonic sound pressure level (1HSPL) were monitored as well.

For varying the geometric parameters, test case C from Table 1, i.e. the 8-bladed SR-2 propeller, which features a straight, unswept blade, was used as the baseline upon which the changes were applied. The propeller was rotated at 6487 RPM in a flow velocity of 204 m/s, similar to the test case by De Gennaro [44]. The inner two thirds of

the blade were left unmodified while the outer third was modified according to the test matrix. The root pitch angle was adjusted to maintain a constant thrust level for all the designs. For sweep and dihedral, the geometry was adjusted by adding a parabolic displacement to the blade such that the tip reached the desired angle while the two third radius point was unchanged and tangency was maintained for a smooth integration of the modification. This was accomplished through eq. (3.1), where r is the radial position, $s(r)$ is the resulting displacement (either sweep or dihedral) non-dimensionalized by radius, $s_0(r)$ is the baseline value, and θ is the desired tip angle. Figure 17 shows an example of the parabolic displacement used. Twist was adjusted similarly except with a simple linear adjustment since tangency was irrelevant to this parameter. Figures are included in each section showing the effect of the geometry modifications on the propeller geometry curves, compared to the baseline shown in Figure 4.

$$s(r) = \begin{cases} s_0(r), & r \leq 2/3 \\ s_0(r) + \frac{3 \tan(\theta)}{2} \left(r - \frac{2}{3}\right)^2, & r > 2/3 \end{cases} \quad (3.1)$$

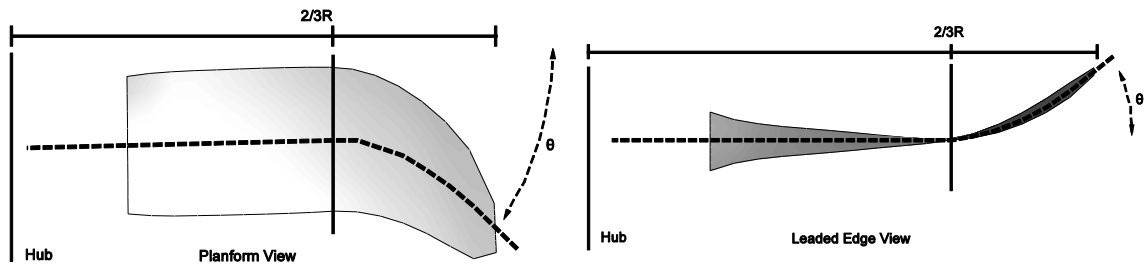


Figure 17. Sweep (left) and dihedral (right) displacement examples.

Tip vortex strength was determined by monitoring the magnitude of the circulation potential stored in the vortex particle emitted by the outermost panel,

covering $R=[0.95, 1.0]$. Noise was registered on a virtual microphone located in the disk plane at a distance of $7.5R$ from the hub, which places it in the far field, as shown in Figure 18. The acoustic pressure-time history recorded at that location was processed through a Fourier transform into an acoustic power spectral plot from which the overall sound pressure level and first harmonic peak could be found.

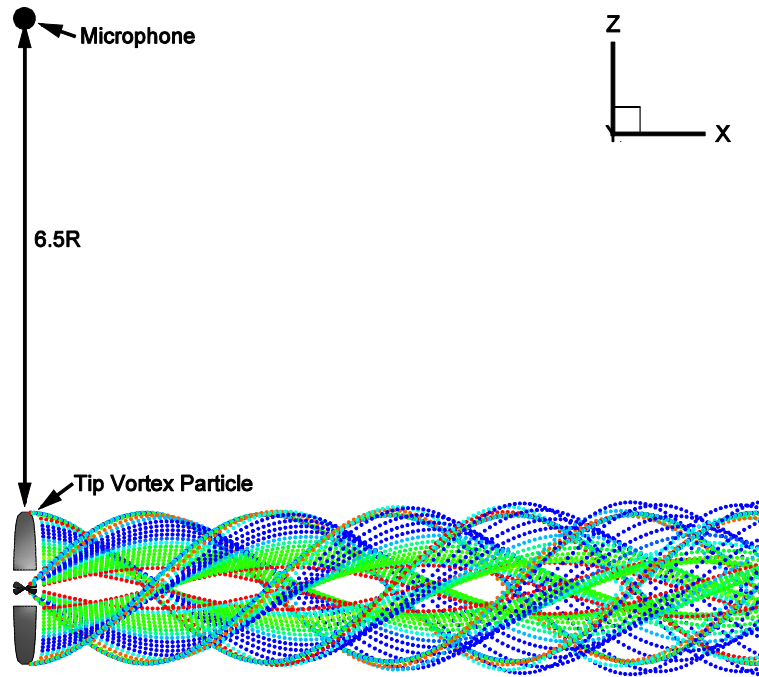


Figure 18. Propeller, wake, and microphone location.

Table 5 shows the ranges and parameters varied for the parametric studies as well as the sections in which their results may be found.

Table 5. Parametric study parameters and ranges.

Parametric Study	Values	Results Section
Tip Sweep	-60, -50, -30, -10, 0, 10, 30, 50, 60	3.2
Tip Dihedral	-60, -40, -20, -10, 0, 10, 20, 40, 60	3.3
Tip Twist	-6, -3, -1.5, 0, 1.5, 3, 6	3.4

3.2. Effect of Tip Leading Edge Sweep

Literature has shown sweep to be effective at mitigating propeller noise for blades with high tip speeds [13]. The chordwise Mach number is decreased by the cosine of the leading edge angle, delaying the onset of thickness-induced shockwaves. It is also possible to sweep the blade in such a way that the acoustic signal emitted by one section of the blade is physically offset from another by half a wavelength at a target frequency and observer angle. This causes the two acoustic signals to interfere destructively and reduces noise. While the former effect will not be demonstrated due to the incompressible nature of the SmartRotor code, and designing explicitly for the latter is a difficult and time-consuming process that is beyond the scope of this research, it is worthwhile mentioning the mechanisms by which sweep affects noise. More to the point of the current research, blade sweep affects both the loading distribution across the blade as well as the way in which the tip vortex is able to form. The range of sweep modifications is shown below in Figure 19.

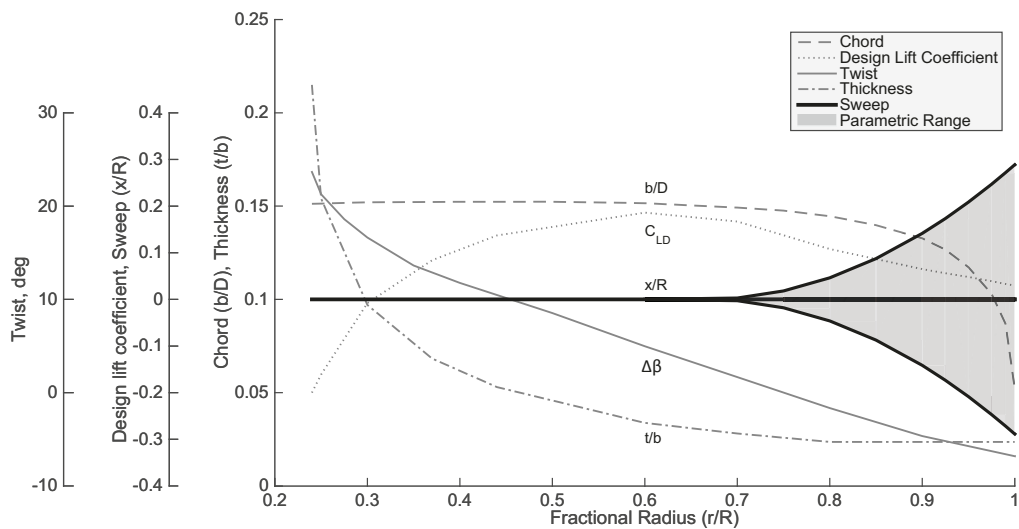


Figure 19. Sweep parametric study geometry curves.

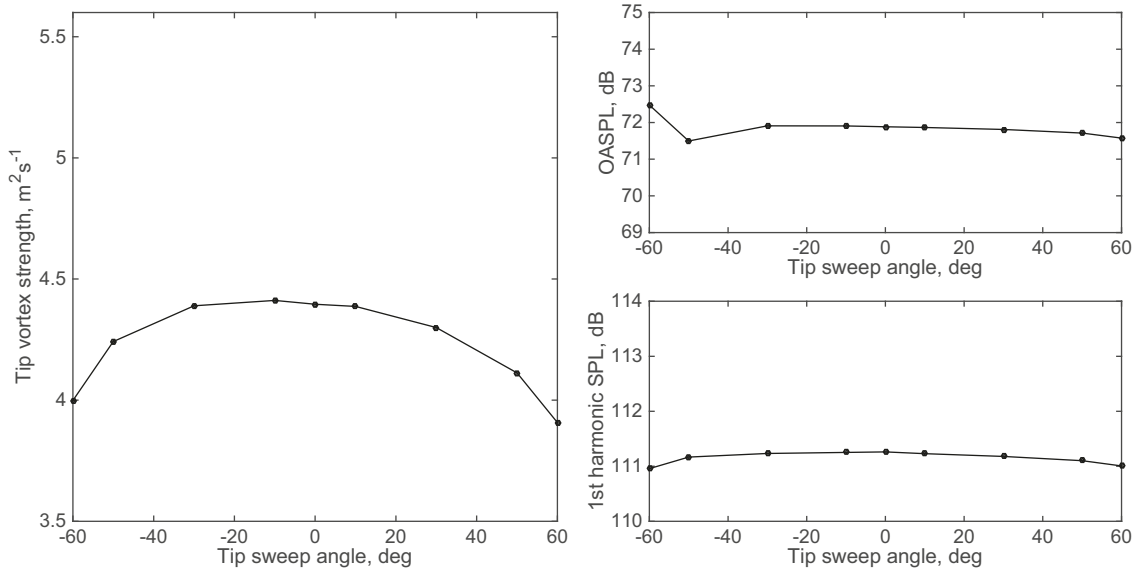


Figure 20. Sweep parametric study results.

The results of the parametric study on tip sweep are shown in Figure 20. As can be seen, tip sweep was relatively effective at managing tip vortex strength. Large absolute values of sweep angles slightly decreased the tip vortex and left the overall sound pressure level (OASPL) and first harmonic sound pressure level (1HSPL) mostly unaffected. Propeller efficiency increased up to 1.5% with forward-swept tips but did not decrease with aft sweep. The change in tip vortex strength stems from the change in relative airflow angle experienced by the swept region of the blade causing reduced loading and circulation. As expected, the inward-shifted loading seen with large sweep angles is accompanied by a decrease in 1HSPL, however slight, in accordance with simplified propeller acoustic models. The effect of sweep would likely be larger if quadrupole noise sources from Mach effects were accounted for (due to the reduced chordwise Mach number caused by sweep), however as the vortex particle method used

in SmartRotor is an inherently incompressible solution this is not possible to accomplish with this code.

Because tip sweep reduced the tip vortex strength by such a magnitude without any adverse effect on noise, it is the most promising parameter for reducing WVI noise without a counterproductive increase in propeller noise.

3.3. Effect of Tip Dihedral

Aircraft winglets are a proven method of drastically reducing the magnitude of the wingtip vortices while simultaneously redirecting their energy in a useful manner. Propeller tip dihedral was examined in the hopes that it would similarly control the tip vortex. While it is acknowledged that the out-of-plane way in which dihedral affects the blade geometry may introduce structural issues when rotating at speed, this has not been investigated by the available literature and is only a possibility whose investigation is beyond the scope of this research. Figure 21 shows the geometry curves used.

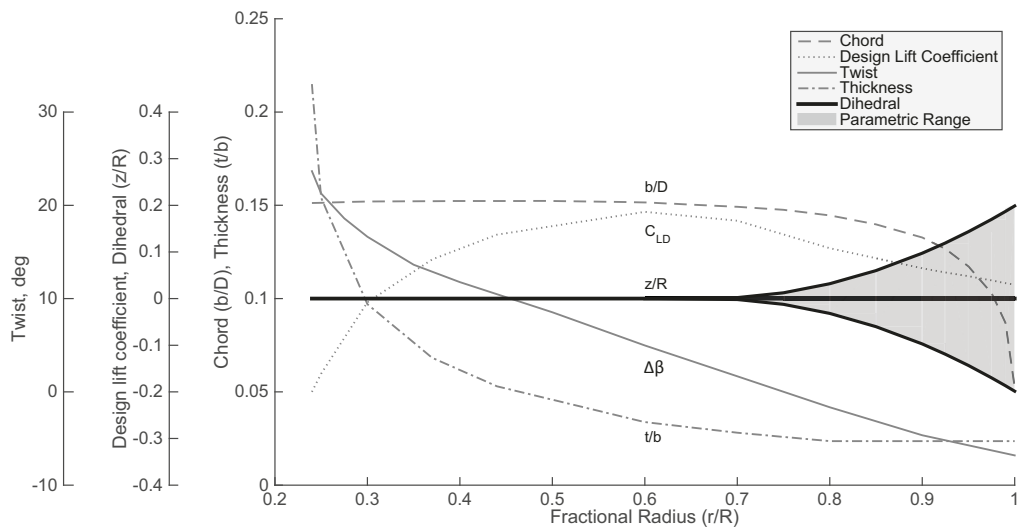


Figure 21. Dihedral parametric study geometry curves.

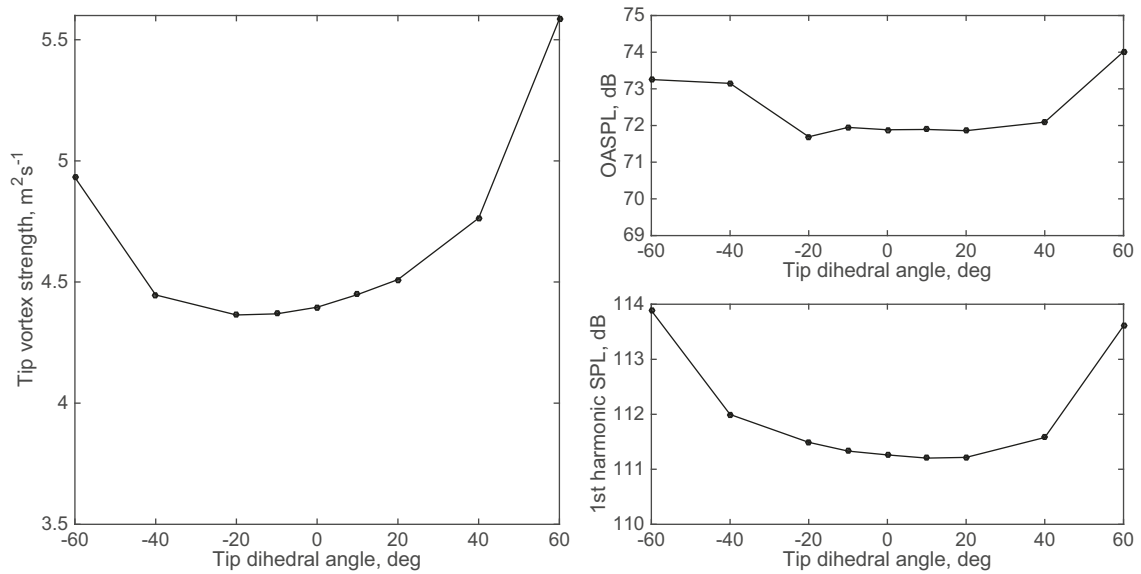


Figure 22. Dihedral parametric study results.

Results of the parametric study are shown in Figure 22. Moderate tip anhedral proved mildly effective at controlling the tip vortex strength but caused a minor increase 1HSPL with only negligible effect on OASPL. It appears that positive dihedral allows the tip vortex to freely roll up and away from the blade while slight negative dihedral (~20 degrees) prevents this by forcing the air downwards and holding the high-pressure region in the concave curve of the blade. This is also implied by the way efficiency does not change significantly across the range examined until 60 degrees of dihedral when it suddenly decreases by 1%. While winglets can generally be viewed as extreme dihedral, anhedral seems to be the more effective direction for propeller blades. This is because of the interaction between the simultaneous twisting in both the dihedral/anhedral direction and the blade twist direction in the rotating frame. The twist near the tip of the propeller causes the upswept portion of the blade to be

somewhat hidden from the incoming airflow as the blade spins as shown in Figure 23 compared to a downswept example.

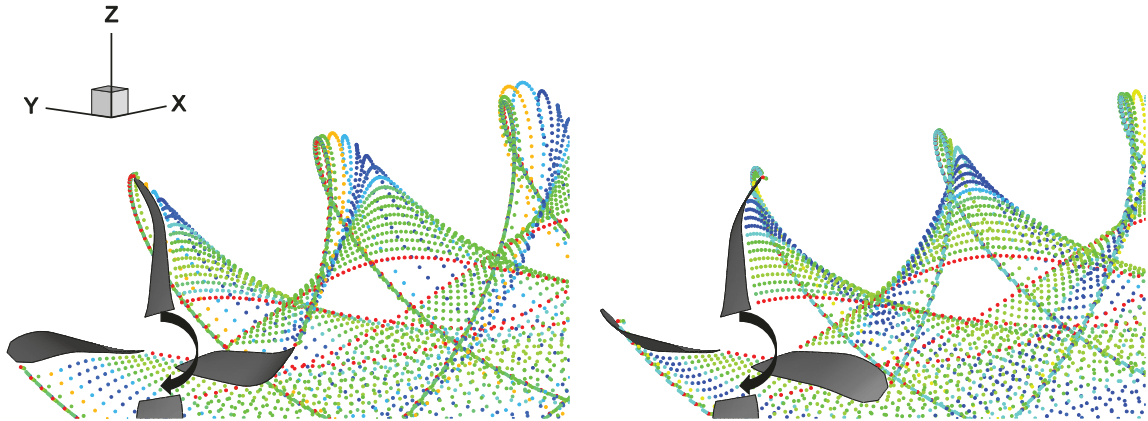


Figure 23. Comparison of wake structure for tip dihedral +40 degrees (left) and -40 degrees (right).

Because negative dihedral successfully reduced tip vortex strength with only a small adverse effect on noise, it is also a promising parameter for reducing WVI noise without a counterproductive increase in propeller noise.

3.4. Effect of Tip Twist

Tip twist was the most effective parameter at managing tip vortex strength on the range examined. Obviously, twisting the propeller tip modifies the loading distribution on that region and could theoretically be used to reduce the tip vortex strength to zero by removing all loading from the tip. Realistically, though, the efficiency losses from such a design would prohibit its usability. As illustrated, along with the results of the parametric study, in Figure 24, this was confirmed by the manner in which efficiency dropped off when tip twist was changed beyond ± 1.5 degrees.

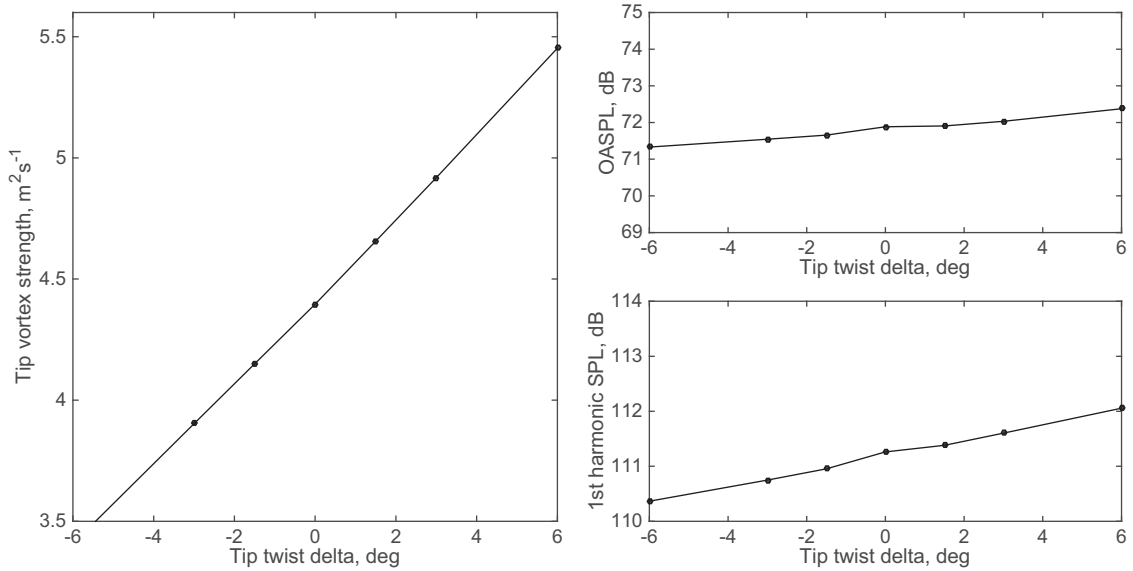


Figure 24. Twist parametric study results with linear twist change.

Modifying the twist towards the tip predictably changes the loading on the blade and so the effect on tip vortex strength is linearly proportional as expected. Shifting the loading on the blade towards the tip by increasing tip twist increased the loading noise as would be predicted by analytical models for propeller noise such as Gutin’s model [1]. Reducing the twist angle towards the tip allowed for weaker tip vortices and quieter blades. Managing the twist of the blade along its entire span instead of only at the tip could capitalize further on this effect.

Tip twist was also varied according to a parabolic function similar to that used for sweep and dihedral. The parabolic change was examined for completeness, even though the first order variation makes more sense in terms design. Figure 25 and Figure 26 show the two resulting geometry curves from the linear and parabolic change, respectively. The linear variation is more effective due to the greater rate at which

loading is shifted towards the hub, necessitating less increase in root pitch angle. The results were very similar, though of reduced magnitude, as seen in Figure 27.

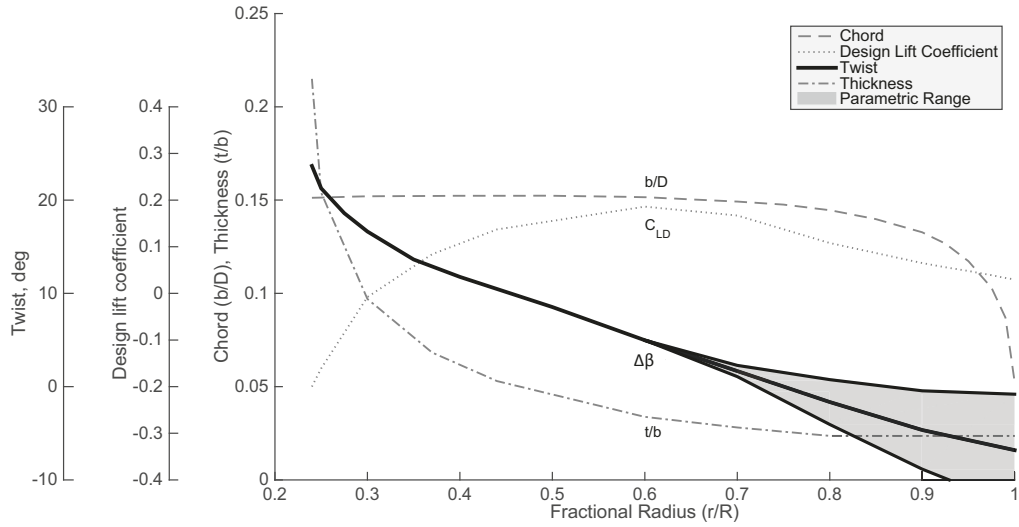


Figure 25. Twist parametric study geometry curves with linear twist change.

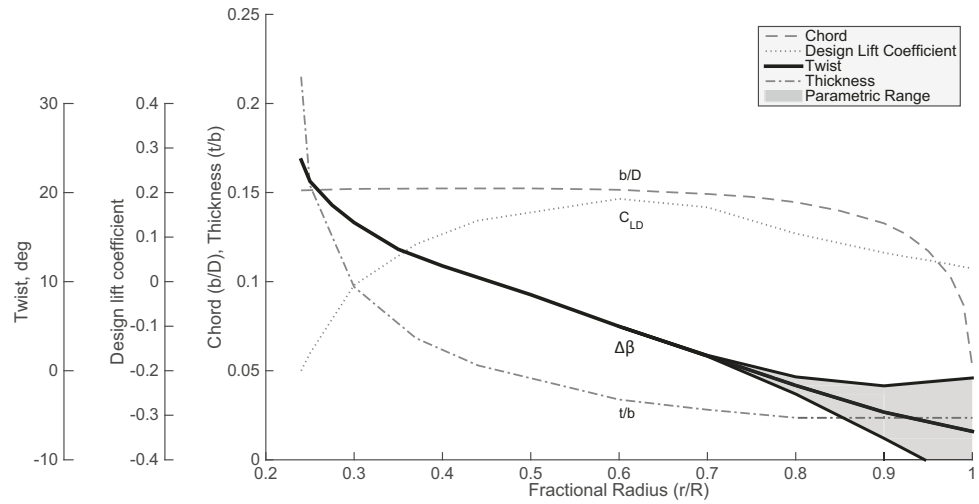


Figure 26. Twist parametric study geometry curves with parabolic twist change.

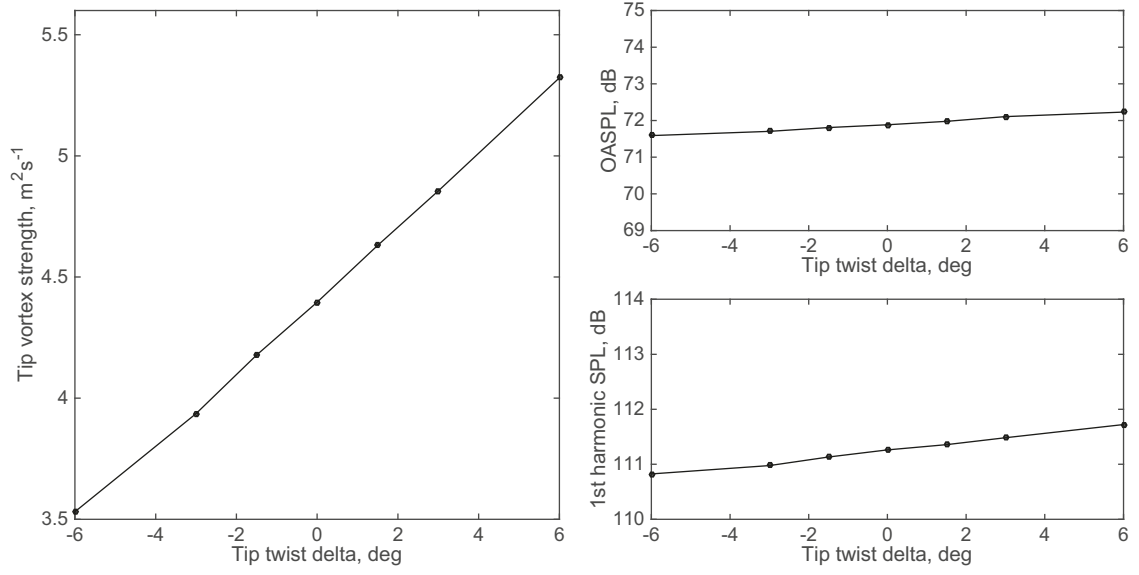


Figure 27. Twist parametric study results with parabolic twist change.

4. Effect of Propeller Vortex-Wing Interference on Noise

4.1. Background

The previous chapter focused solely on a propeller in isolation. This is never the case in the real world as the propeller is always mounted somehow to an aircraft. This chapter investigates the acoustic effect of a traditional tractor-type configuration with a wing in the wake of the propeller. This will undoubtedly change the acoustic signature, as there is the added periodic change in wing loading as the wake of each blade passes across the wing as well as the random nature of the propeller's wake and tip vortex interacting with the lifting surface.

It has been theorized that this interaction could contribute significantly to both cabin and exterior noise through various mechanisms. As mentioned previously, the periodic nature of the propeller's wake is thought to be able to excite the skin panels on the wing and thus transmit noise through the aircraft's structure. More to the point of the current research is the similarity to rotorcraft blade-vortex interaction (BVI) wherein, depending on the forward speed of the helicopter, the leading edge of one blade impacts the vortex from the preceding blade at varying angles. The relationship between the sound pressure level generated by this impact and the relative angle of the blade and vortex has been well established [58]. Similarly, for propellers, depending on the relative placement of the wing and propeller, and the aircraft's forward speed, the angle between the propeller's vortex and the wing's leading edge also changes. For example, if the propeller axis is in line with the chord line of the wing, the vortex will

impact nearly orthogonally, whereas if the engine is mounted sufficiently below the wing the tip vortex will impact closer to parallel to the leading edge as shown in Figure 28. This effect, as well as the effect of varying the downstream position of the wing to allow the propeller's wake to develop or dissipate, as the case may be, will be specifically investigated in this chapter.

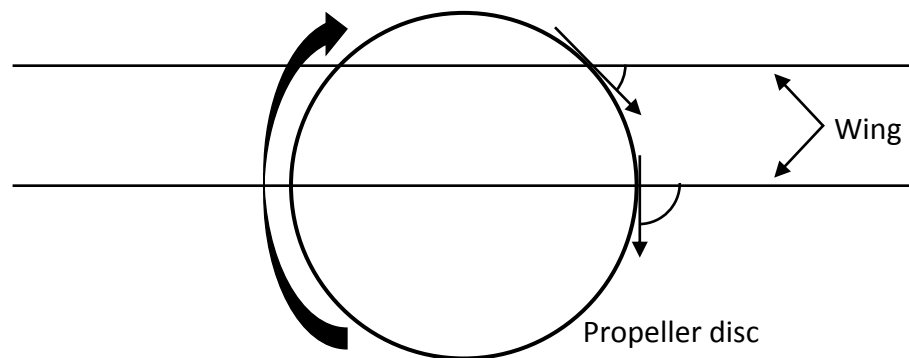


Figure 28. Illustration of the effect of wing vertical position on vortex impact angle.

As it is not always possible to locate the wing relative to the propeller in the most preferred manner, other mechanisms of mitigating the effect of VWI noise will be investigated. The relative angle of the vortex and leading edge can also be changed by adjusting the local leading edge sweep of the wing at the location where the wake passes over it. Several possible leading edge shapes and their associated noise and aerodynamic performance will be presented.

Finally, the influence of the entire propeller, nacelle, and wing configuration will be investigated. No longer will the propeller and wing be operating in isolation. Now the presence of a non-lifting body downstream of the propeller will influence the formation and deformation of the propeller wake as well as the way in which it interacts with the

wing. Although the effect is minor, this will offer some insight into further noise mechanisms.

4.2. Baseline Results

The same simulation from test case C, from Table 1, was used with a simple wing placed in the wake of the propeller. The propeller used was again the 4-bladed SR-2 propeller spinning at 6487 RPM in a flow of 204 m/s. The baseline wing was implemented as a thin wing body with a chord equal to 0.8 blade diameters. The wing was located 0.8 chord lengths downstream and in line vertically with the propeller axis. Its span was six blade diameters in length such that the effect of the wing's own tip vortices would not interfere with the propeller's wake. The wake particles from this arrangement are visualized in Figure 29. While the wing has been modeled as a thin wing in this work, its significant difference in size and thickness compared to the propeller blades means that more accurate results could possibly be obtained by modeling it as a thick wing to force the vortex particles to deform around it more realistically, although that will be left to future investigation due to the complexity of modelling it as such.

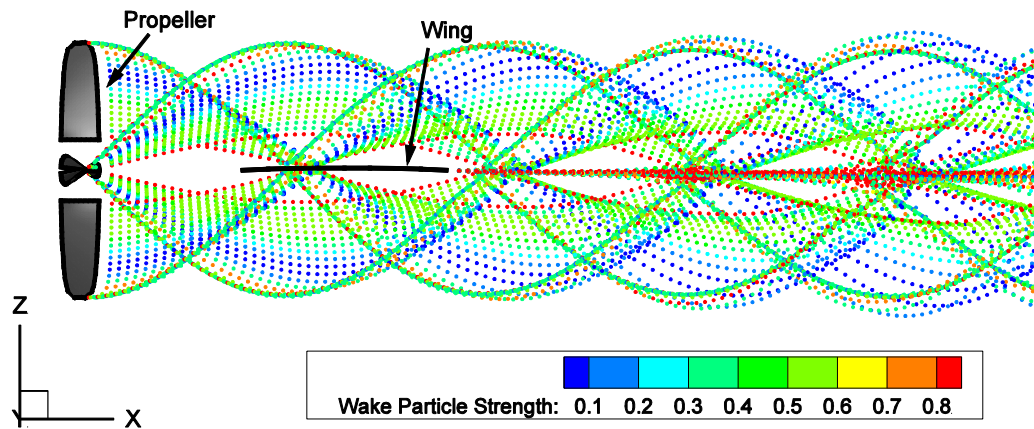


Figure 29. Wake particle visualization of the baseline WVI case.

The acoustic spectral density plot of the baseline WVI case as compared to the isolated propeller case is shown in Figure 30. Of particular note is that the 1st harmonic sound pressure level remains virtually unchanged while the overall sound pressure level has drastically increased by 2.6 dB. This implies that the primary driver of WVI noise is the mass interaction of the chaotic wake structure with the wing surface as opposed to a cohesive periodic interaction from the propeller tip vortex. This is not to say that the tip vortex is not a significant factor in WVI noise, instead this means that if it is, the noise mechanism is more the cutting of the vortex core and less the fluctuating loading imposed on the wing.

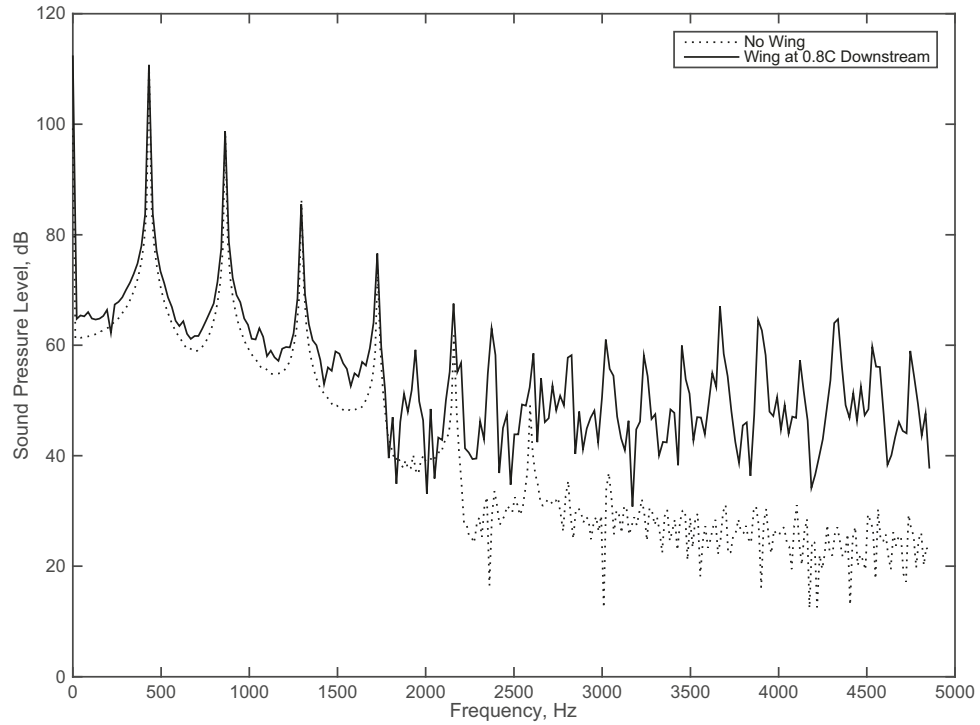


Figure 30. Comparison of WVI baseline case and isolated propeller.

The wing also has a significant impact on the propeller wake structure, as expected. While the wake is perfectly helical upstream of the wing, it tends to compress on the sides where it rotates into the wing surface. The wake then deforms towards the compressed side and flattens as it moves downstream. This behaviour is seen in Figure 31.

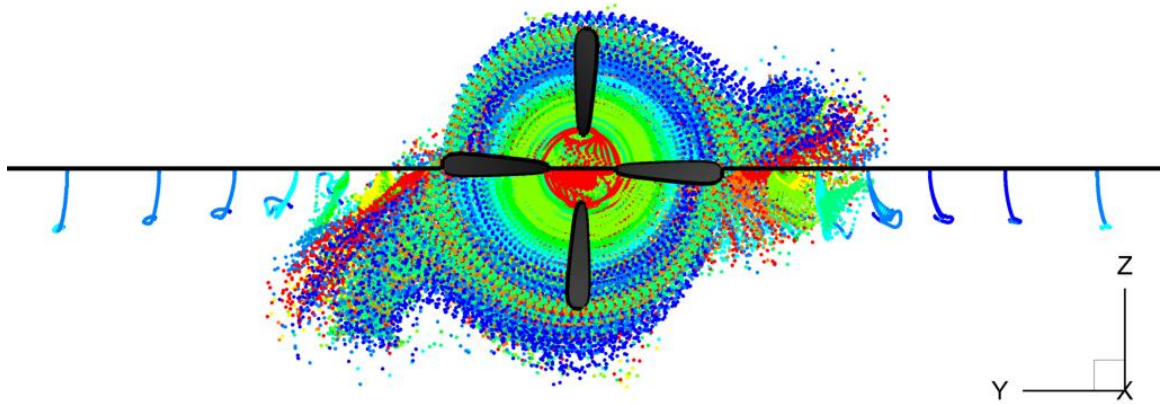


Figure 31. Front view of the developed wake showing the flattening effect of the wing surface.

The propeller and wing are seen to have mutual, cyclical effects on each other. The wing's lift coefficient is slightly elevated from the wing alone case and fluctuates slightly with time as the propeller's forced air moves across it. The propeller's thrust similarly fluctuates with time as a result of the wing's influence.

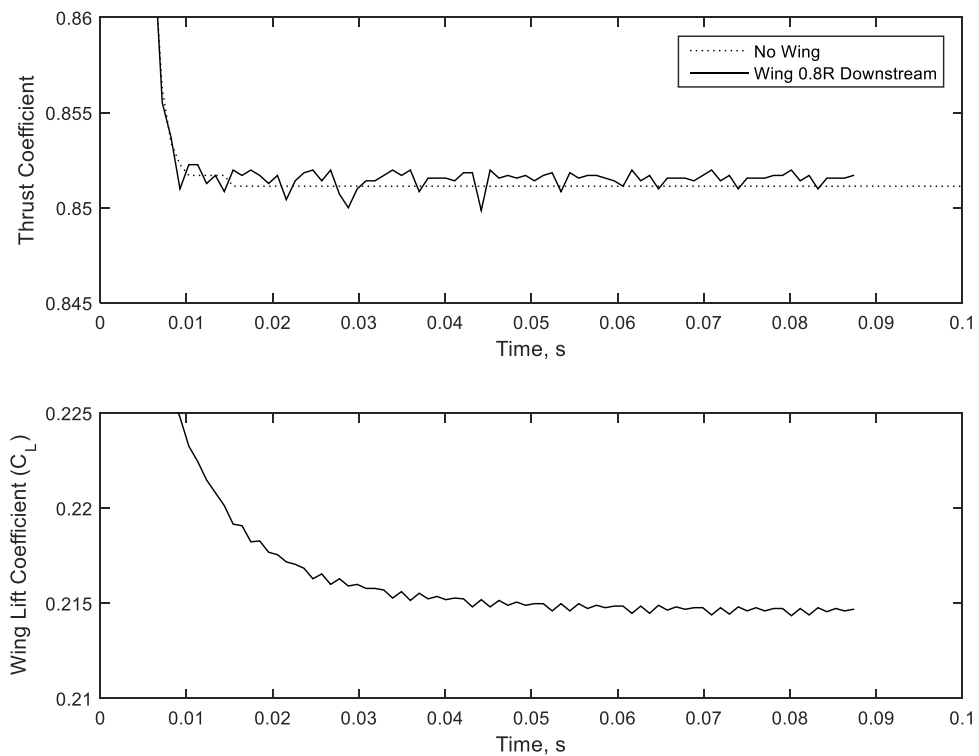


Figure 32. Wing/propeller mutual interference effects.

4.3. Effect of Tip Vortex Strength

In order to make an attempt at differentiating between the propeller tip vortex noise source and that of the disc's wake, the baseline WVI case was modified to use the endpoints of the twist parametric study (± 6 degrees of tip twist change). This allowed the trading of energy between the disc wake and the tip vortex through increased or decreased tip loading. This showed only a marginal change in OASPL, on the order of 0.3 dB, but a more significant change in 1HSPL, of approximately 1.2 dB. This implies that the propeller's wake is the main cause of VWI broadband noise but the more concentrated tip vortex is responsible for the tonal component.

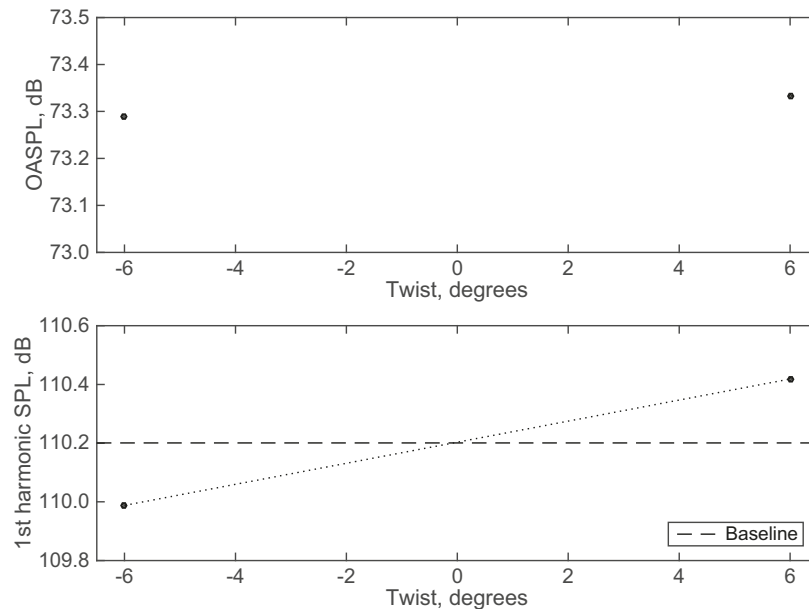


Figure 33. Effect of propeller tip twist on WVI noise at the baseline wing position.

This effect is even more pronounced when the wing is displaced vertically to $1.0R$. At this position, the angle between the tip vortex core and the wing's leading edge is minimized and so VWI is maximized. Here the OASPL does not change while the first harmonic SPL changes by more than 4 dB as shown in Figure 34.

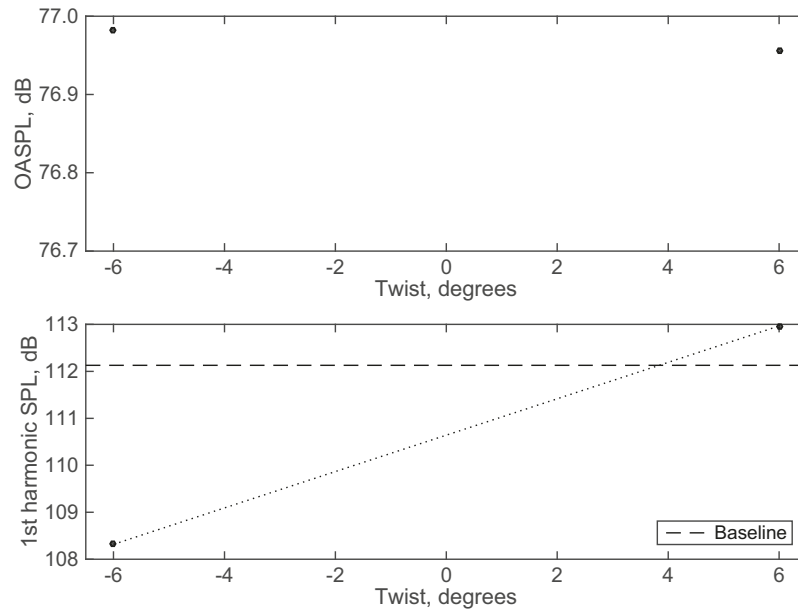


Figure 34. Effect of tip twist on noise at a vertical position of 1.0R.

4.4. Effect of Wing Placement

Having established baseline results for the simple wing interference case, the effect of the wing's placement was considered. The downstream positioning of the wing affects the degree to which the propeller's wake is established or dissipated while the vertical positioning of the wing affects the radial intersect chord length where the wake impacts the wing as well as the mutual angle between the helical vortex and the wing's leading edge.

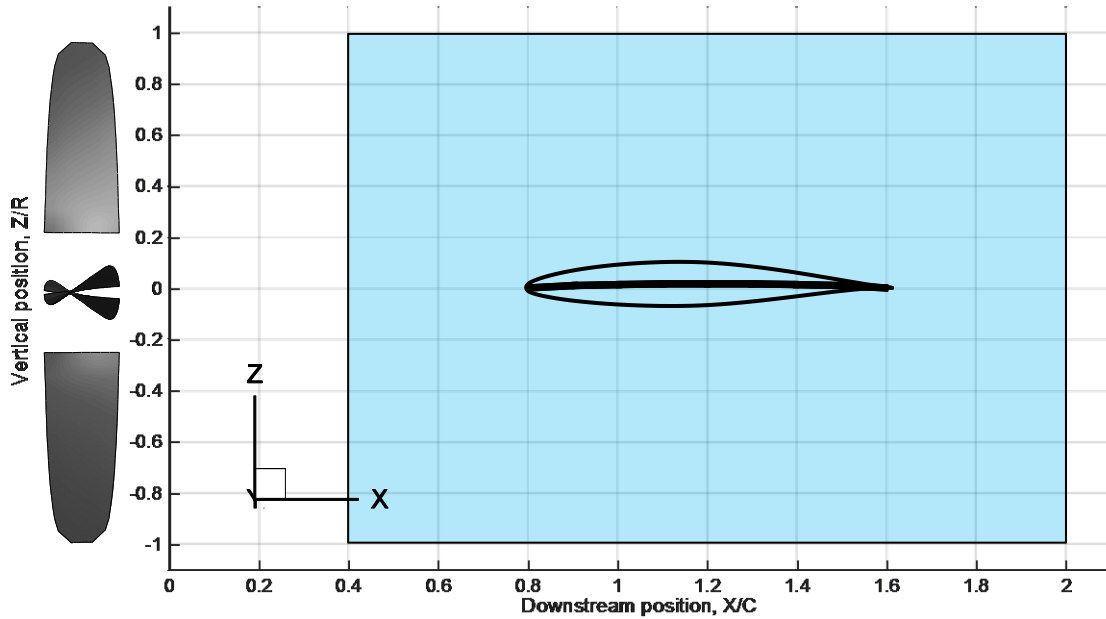


Figure 35. Wing leading edge position downstream and vertical range.

Multiple simulations were run with the wing located in various positions. The position of the wing's leading edge was varied from $0.4C$ downstream to $2.0C$. It was positioned vertically between $1R$ above and below the propeller's axis. The results will not be symmetric above and below the axis because the wing is a lifting surface and has induced circulation of its own that change the leading edge inflow angle of the surrounding flow.

Examining the effect of downstream position only, while the vertical position is fixed at the propeller axis, shows the effect of the wake's development on noise. Both harmonic noise and OASPL changed by less than 2 dB on the range examined. This is because the wake is already mostly fully developed by the time it reaches the wing and does not begin to dissipate until far downstream.

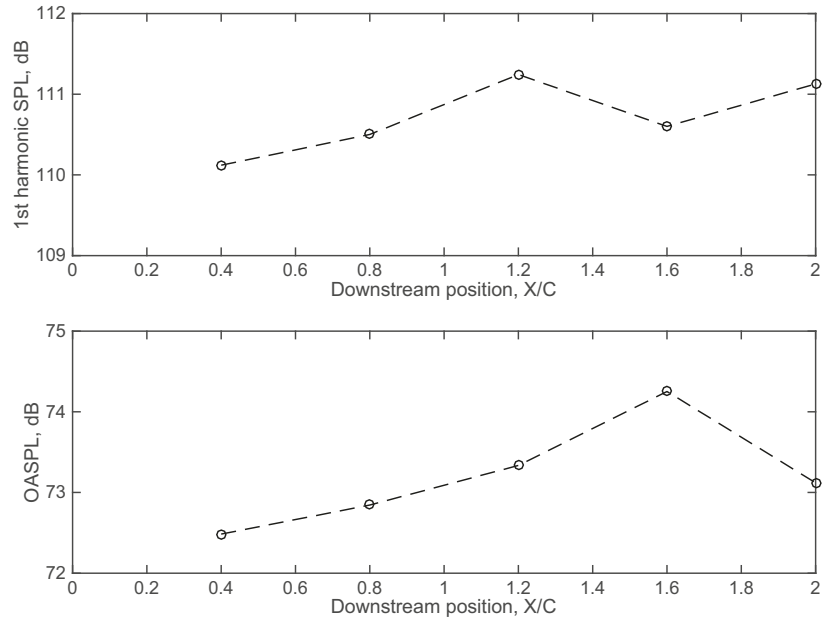


Figure 36. Effect of wing downstream position on noise.

Varying only the vertical position similarly shows the effect of the vortex-wing angle and radial intersect chord length of the wing-wake interaction region. As illustrated in Figure 37, the harmonic noise is minimized when the propeller axis is on the wing plane – i.e. when the wake movement is orthogonal to the wing’s leading edge. The overall sound pressure level shows a peak at this location, however this is likely due to the root vortex also impacting the wing in this configuration.

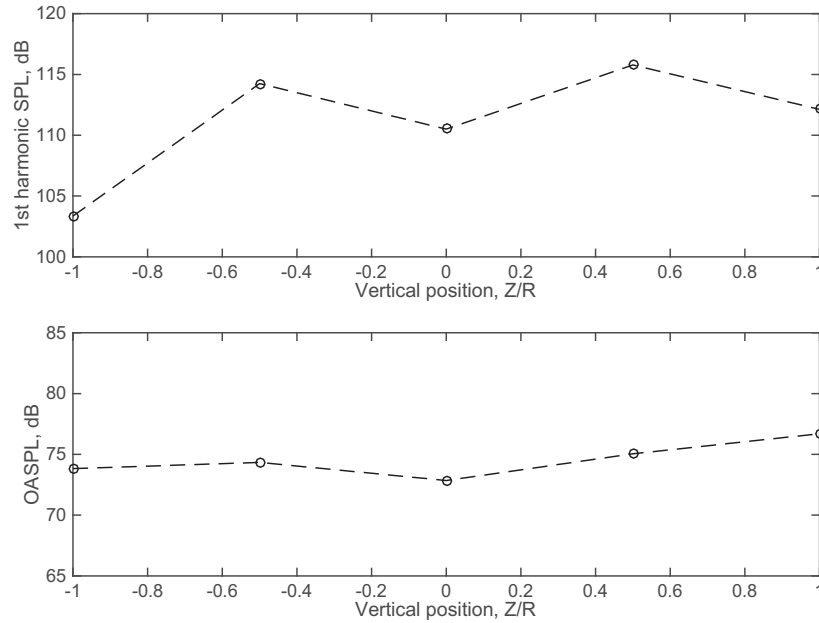


Figure 37. Effect of wing vertical position on noise.

Visualizing the results of the whole region analyzed shows the areas where the interaction noise is lowest. First harmonic sound pressure level is generally lowest on the propeller axis, although a sweet spot seems to exist near $1.2C$ downstream and $0.5R$ above or below the propeller axis that reduces 1HSPL by up to 15 dB. This appears to be a result of destructive interference between WVI noise and propeller noise at the particular microphone location. Overall sound pressure level increases when the wing is moved off of the propeller axis. This is because moving the wing off the axis makes the mutual angle between the wing's leading edge and the propeller tip vortex non-orthogonal, leading to increased WVI noise [58]. This hypothesis is strengthened by the results of varying leading edge sweep that will be presented later.

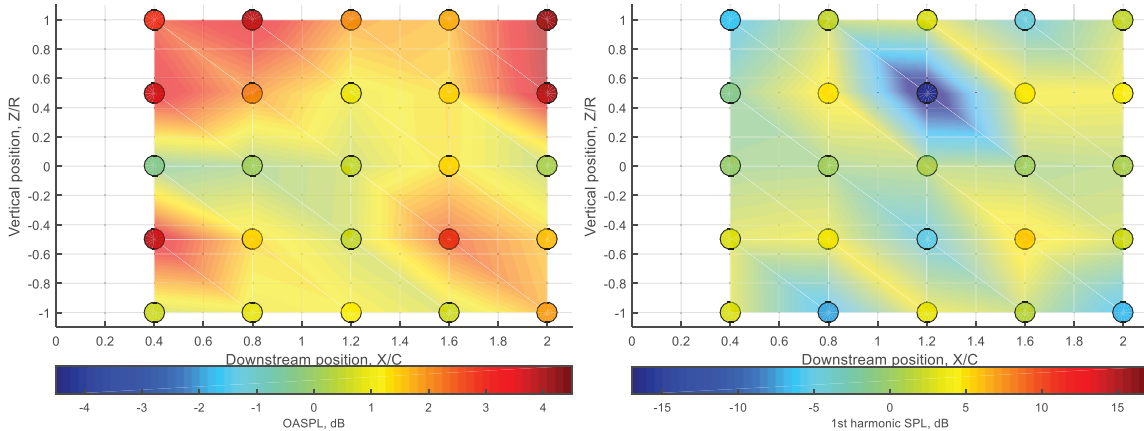


Figure 38. OASPL and 1HSPL change with wing position from baseline case (0.8C/OR).

4.5. Effect of Wing Local Leading Edge Sweep

A more direct approach to modifying the relative angle between the wing's leading edge and the propeller's helical tip vortex is to adjust the leading edge sweep of the wing in the region where it is intersected by the wake. Changing the shape of the wing's leading edge line could be less intrusive to aircraft designers than wholesale modification of the engine placement.

Several possible leading edge shapes were examined. While the optimization of these shapes is beyond the scope of this work, the curvature roughly correlates with the intensity of the vortex particles impacting the wing at that point. This is done to attempt to maximize the mutual angle between the leading edge and the vortex core in the places where VWI noise is likely to be highest. Figure 39 shows the various leading edge shapes used at the three vertical positions examined. It is worth noting that when the wing is in plane with the propeller axis, the vortex is always orthogonal to a straight leading edge. The shapes from the 0.5R position were used there as well for

completeness and to verify the belief that little change in acoustic pressure levels would be observed.

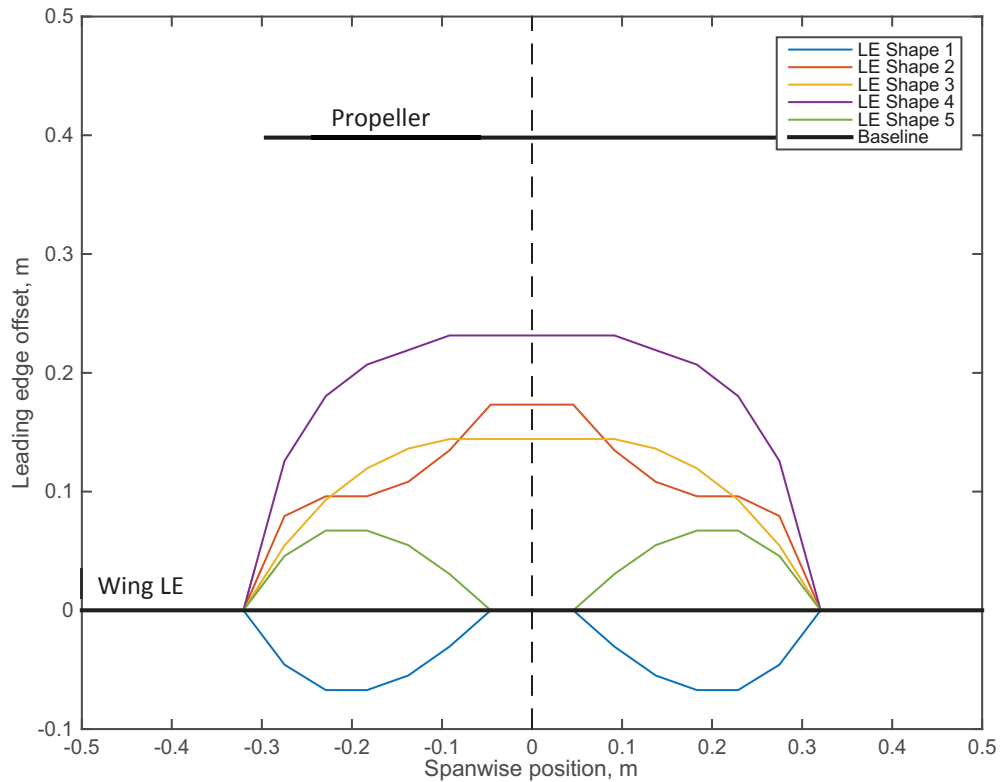


Figure 39. Leading edge shapes.

Note also, that the mutual angles reported below apply only to the examined advance ratio. If the rotational speed or the forward speed changes, so too does the mutual angle and the noise generated. This means that this potential method of reducing WVI noise is most effective at the design condition. Off-design condition effects are beyond the scope of this section, and could be examined in future research.

In the case where the wing is in plane with the propeller axis, only marginal effects on noise are seen. OASPL and 1HSPL changed by less than 1dB across the designs. This is as expected as the actual angle between the wing and vortex varies little

across the various leading edge designs, from 75.39° with design 4 to 79.06° with design 5; with the baseline remaining orthogonal (90°). The hypothesis that lower relative angles increase noise is supported by the acoustic results shown below.

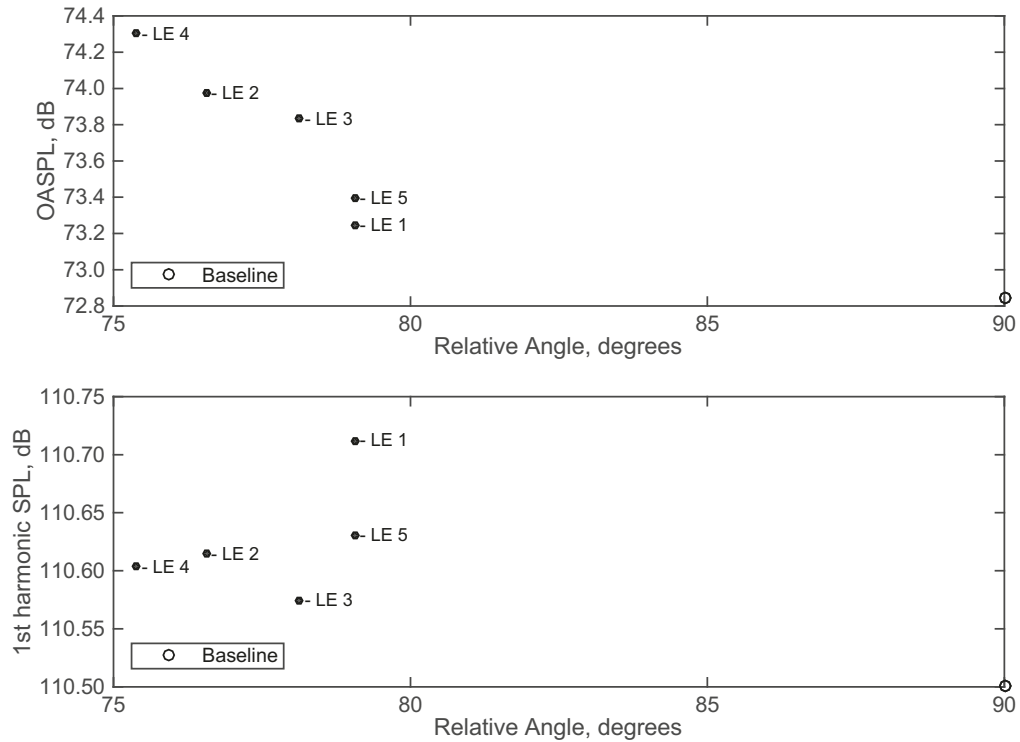


Figure 40. Effect of leading edge shape on noise with wing on propeller axis.

Next the wing was moved 0.5R vertically and the same leading edge designs were examined. Here it was found that the first harmonic noise had an inverse correlation with leading edge angle while broadband noise was more closely related to the resulting gap between the leading edge and propeller. OASPL varied by up to 3 dB between the quietest and loudest variant and 1HSPL by up to 7.5 dB. One feature of note was that those designs with very high leading edge angle (and correspondingly reduced propeller-LE gap) succeeded in reducing their 1st harmonic sound pressure level by redirecting the acoustic energy into the 2nd harmonic of BPF, as shown in Figure 42.

Defining the relative angle between the vortex core and the wing's leading edge becomes more difficult when the wing is off the propeller axis due to the fact that the up-going side of the vortex is not parallel to the down-going side. Thus, the relative angle will be different depending on which side is examined – up to almost 30 degrees among the designs studied. The values reported below are the average of the up-going and down-going vortex-wing angles.

While OASPL increased in some cases – those where the leading edge moved significantly closer to the propeller disk – the 1HSPL generally decreased with increasing the relative angle between the leading edge and the vortex core.

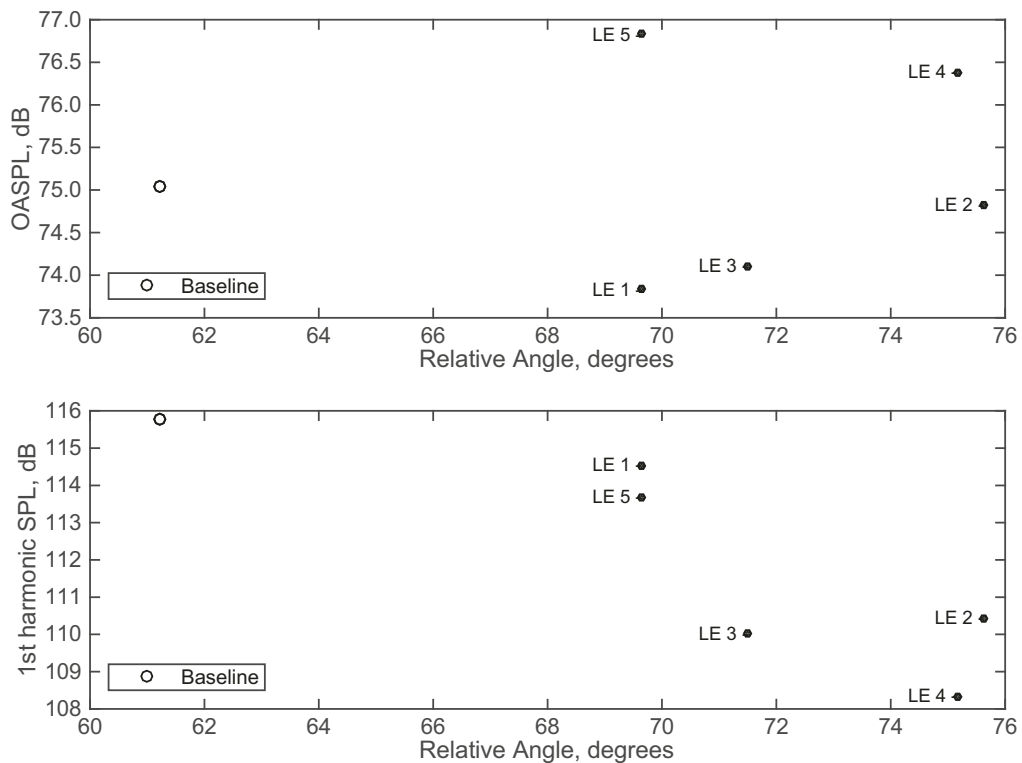


Figure 41. Effect of leading edge shape on noise with wing 0.5R above the propeller axis.

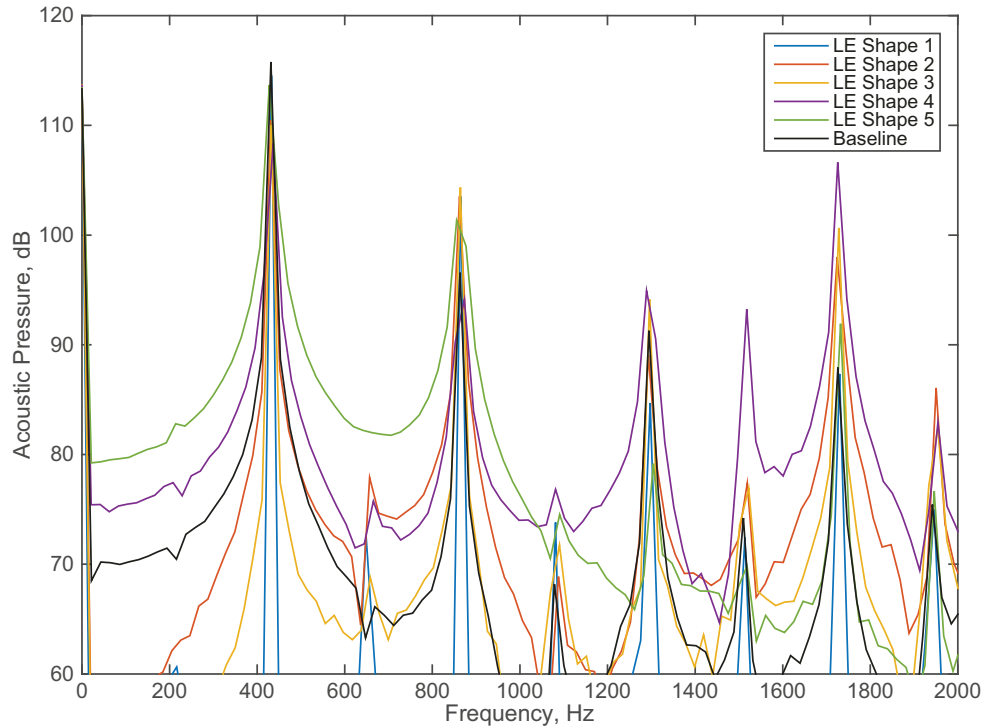


Figure 42. Shifting of sound pressure level to the second harmonic seen with high LE sweep.

When the wing is positioned tangent to the upper edge of the propeller's wake, at $1.0R$, most leading edge designs were found to reduce 1HSPL and increase OASPL when compared to the baseline. The increase in OASPL, however, was very slight, on the order of 0.5-2dB. With the exception of designs 1 and 5, 1HSPL was reduced by 3-6dB, although this is more likely due to destructive interference than legitimate aeroacoustic effects. At this vertical position, the mutual angle of the leading edge and tip vortex has become the same for all designs as they all feature a straight center. This is why the effect of leading edge shape here is less pronounced than at $0.5R$ above the propeller axis.

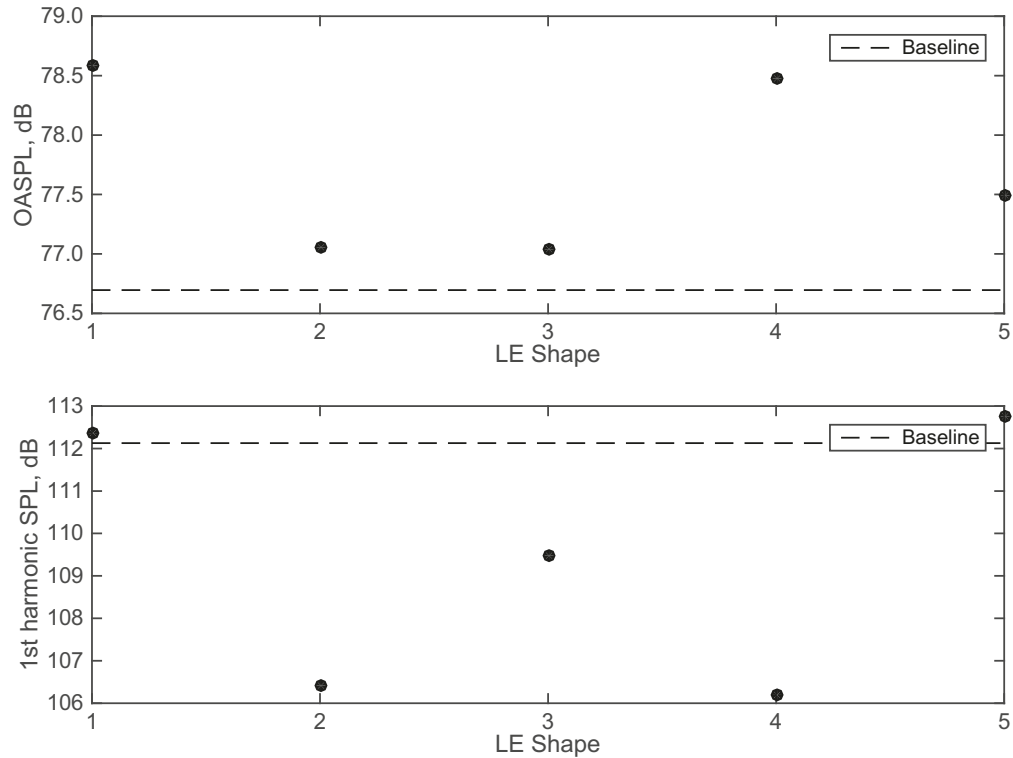


Figure 43. Effect of leading edge shape on noise with wing 1.0R above the propeller axis.

4.6. Effect of Complete Propeller, Nacelle, Wing Configuration

As a final note on the investigation of wing/propeller integration a representative nacelle and spinner were added to the baseline simulation. For a given point on the surface downstream of the propeller, the pressure should fluctuate with the blade passage frequency and the deformation induced on the wake by the surface. In accordance with the Farassat 1A formulation (eqs. (2.21)-(2.23)), both these effects will generate some noise. The aim of this section is to determine the extent of the added noise due to the nacelle and spinner.

The nacelle and spinner were modeled in SmartRotor as non-lifting bodies of revolution. Their geometry was based on the nacelle of the Bombardier Q400 turboprop passenger airliner [59] and is shown in Figure 44 along with the rest of the configuration

and associated wake. The nacelle was fixed in space while the spinner rotated at the same rate as the propeller. It was necessary to move the wing upward from the surface of the nacelle so as not to create mathematical singularities where the two panels met. The fact that the wing and nacelle do not physically attach in the simulation is justified as the wing body merely represents the chord line of the wing and its actual thickness would meet the nacelle.

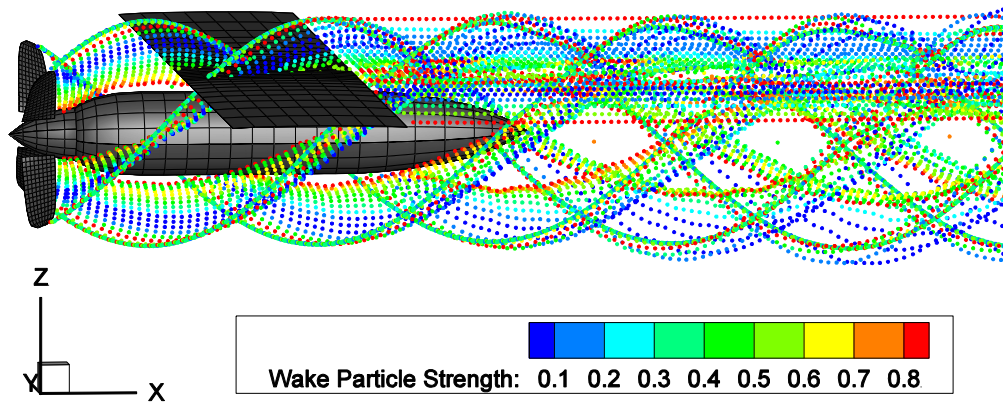


Figure 44. Full configuration wake visualization.

This simulation was run at the same cruise configuration as used in the WVI study. The propeller and spinner rotate at 6487 RPM and the forward speed is 204 m/s.

The acoustic spectrum of the full configuration under these conditions is shown in Figure 45. As expected, the harmonic noise is virtually unchanged, as this has been shown to be primarily generated by the propeller loading, with minor contributions from the tip vortex-wing interaction. The broadband noise has increased slightly from the addition of the nacelle and spinner. This is expected to happen with more geometry panels emitting noise from their fluctuating loading in the presence of a wake.

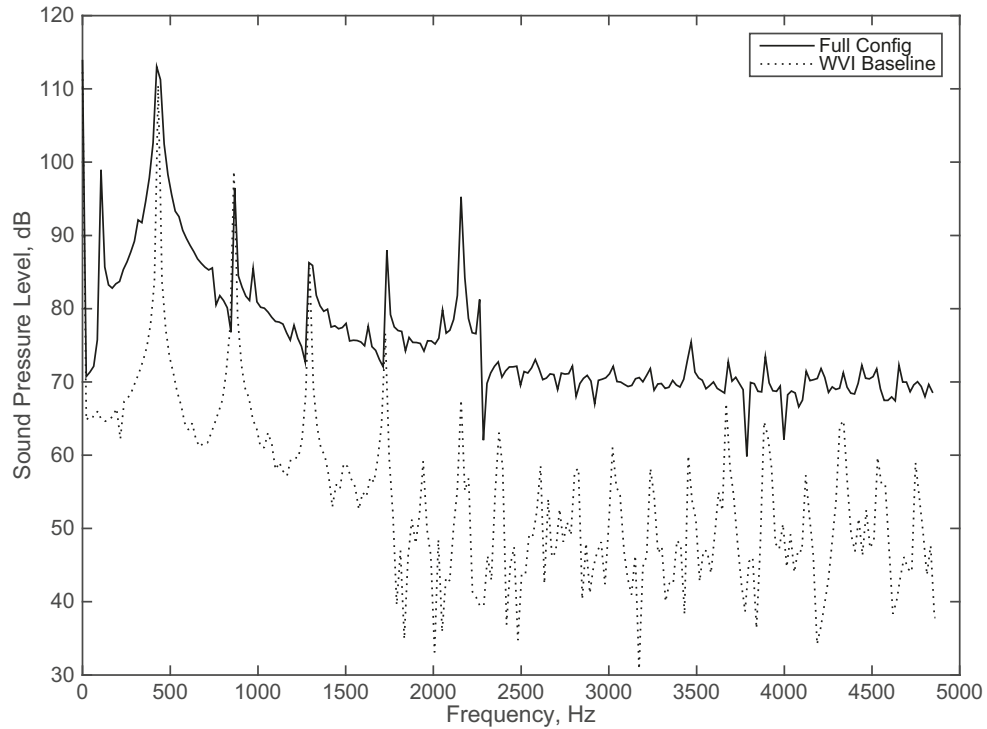


Figure 45. Acoustic spectrum of full configuration.

Overall, the effects of the nacelle and spinner are minor, stemming mostly from the addition of more broadband-emitting noise surfaces. Given that the nacelle is located where the wake is weakest and does not direct much additional flow toward the wing, this is to be expected. This, and the fact that the propeller and wing have aerodynamic forces orders of magnitude higher than the spinner or nacelle, means that neglecting the nacelle is a reasonable approximation to reduce computational load.

5. Effect of Off-Design Conditions on Noise

5.1. Background

Until this point, the simulations have all taken place at, or near, one of the design points of the propeller. This is often the (non-trivial) best-case scenario for noise and efficiency. Unfortunately, the time when noise regulations are most demanding – during takeoff and landing – is not at the design point. While improvements made at the design point will be beneficial to passengers and crew and will contribute at least slightly to reductions in noise at off-design conditions, they do not necessarily reduce noise for bystanders under non-cruise.

Off-design conditions, particularly non-axial inflow, introduce a noise source from non-constant loading on the blades of the propeller. In the case of angle of attack or yaw angles, as a blade rotates through azimuthal angles, the inflow angle varies accordingly. This in turn affects the instantaneous loading on that blade, which, as seen in the Farassat 1A formulation, generates noise.

Little research is available in the published literature on the effect of off-design conditions. What is present focuses primarily on the effect of angle of attack. Note that for an isolated propeller, angle of attack and yaw angle are equivalent. Dittmar et al. [6], [7] performed aeroacoustic experiments with various SR- series propellers at 2 and 4 degrees angle of attack. They found that noise increased by up to 9 dB with higher angles of attack for certain microphone positions. They concluded that the upwash induced by a wing could cause a similar effect and corresponding increase in noise. An

analytical method for predicting the effect of angle of attack on propeller noise was derived by Krejsa [15], based on the analytical models of propeller noise presenter earlier.

This chapter will first examine the effect of high angle of attack, yaw (crosswind), and low forward speed on the baseline wing/propeller case from the previous chapter.

5.2. Effect of Non-Axial Inflow

The baseline WVI simulation from the previous chapter was modified to have a 3- and 6-degree angle of attack and 3- and 6-degree yaw angle. The angle of attack will be compounded by the increased lift of the wing generating a further non-uniformity in the propeller's inflow. Yaw, while not affecting the propeller's inflow in the same way, will affect the relative angle between the propeller's wake and the wing.

5.2.1. Angle of Attack

The acoustic spectrum for the three angle of attack cases is plotted in Figure 46. While the first harmonic remained mostly unaffected, the second and higher harmonics increased with higher angles of attack. OASPL also correlated with change in angle of attack, increasing by 3.5 dB at 3° and to 5.4 dB above the baseline at 6° angle of attack.

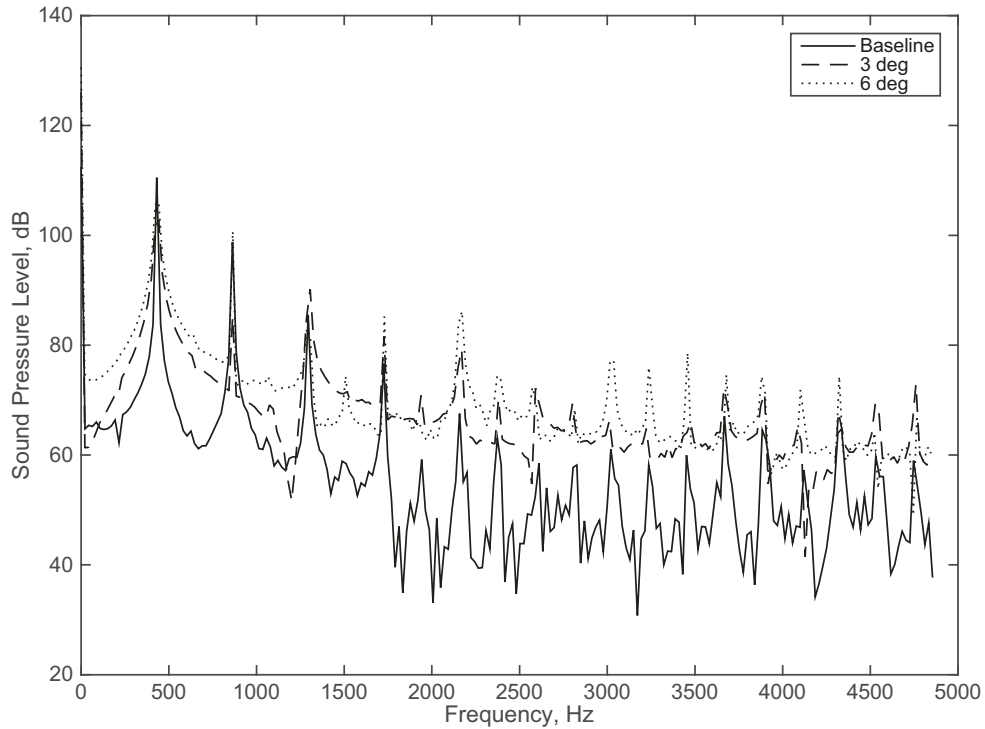


Figure 46. Acoustic spectrum of varying angles of attack.

5.2.2. Yaw Angle

The effect of yaw angle is very similar to that of angle of attack. Again, the first harmonic remained unchanged, with increases visible in the higher harmonic peaks. OASPL increased with increasing yaw angle, although with less magnitude than seen when changing angle of attack. In this case, a yaw angle of 3° increased the OASPL by 2.4 dB and 6° of yaw increased OASPL by 3.0dB above the baseline level. The reason for the greater effect of angle of attack on OASPL compared to yaw angle is that the inflow angle to the propeller is exaggerated by the induced upflow caused by the wing that is not present when changing yaw angle.

Note that both angle of attack and yaw angle had a greater effect on higher frequencies, especially the fifth harmonic of the blade passage frequency, while the first

harmonic was unaffected. While an investigation of why the fifth harmonic is so affected is beyond the scope of this research, it has been shown analytically in literature that higher modes are more affected by the non-axial inflow [15].

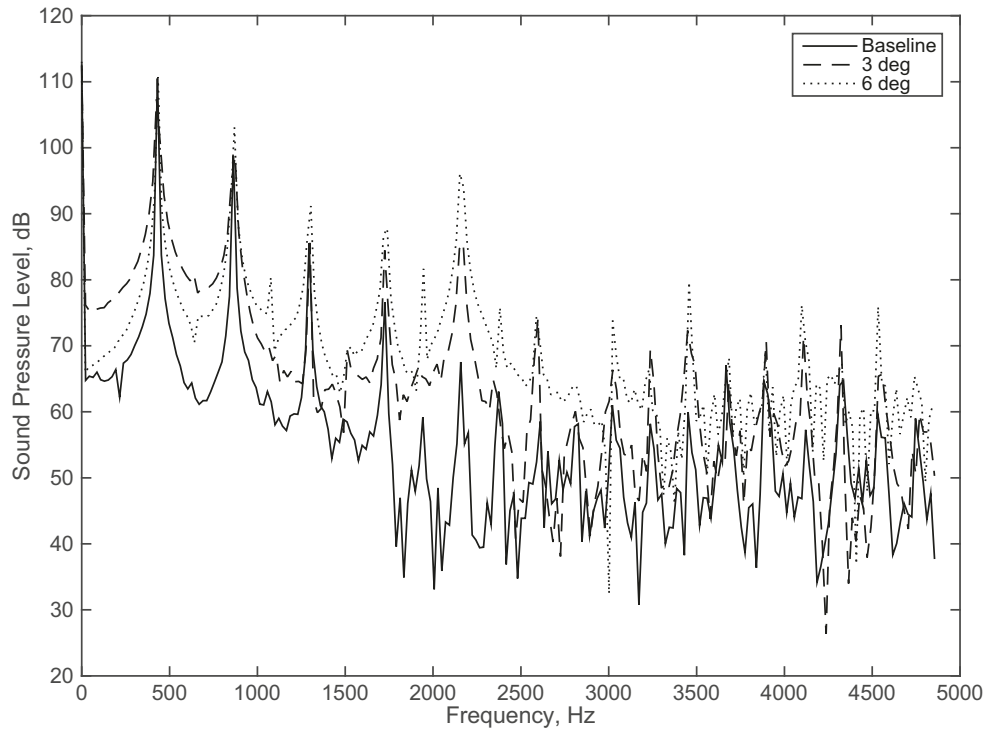


Figure 47. Acoustic spectrum of varying yaw angles.

5.2.3. No Forward Speed

The propeller/wing configuration was simulated with no exterior velocity field to investigate the noise under takeoff conditions compared to cruise. The rotation speed and root pitch angle were left unchanged from the cruise condition so that the frequency spectra could be compared directly. While leaving the root pitch angle and rotation speed constant at zero airspeed is likely not the use case for most real aircraft, the ability to compare the acoustic spectra was deemed more important in providing insight into the effect of forward speed on noise.

It was necessary to run this simulation for a much longer period of time so that the initial roll-up of the wake could pass beyond the wing and so that the wake could form some semblance of periodicity. This situation is where SmartRotor begins to lose its computational advantage in that as the number of time steps increases, the calculation time per time step increases roughly at the second power.

It was again observed that the harmonic peaks were dominated by the noise from the propeller itself and that the peaks were largely unchanged. The broadband noise level drastically increased, adding to the SPL of the second and third BPF peaks before masking all higher frequencies. Figure 48 shows the resulting acoustic spectrum compared to the baseline cruise WVI case. The chaotic nature of the propeller's wake interacting with the wing results in the much higher broadband noise seen here. The wake structure at zero airspeed, visualized in Figure 49, is much less coherent than that seen at cruise.

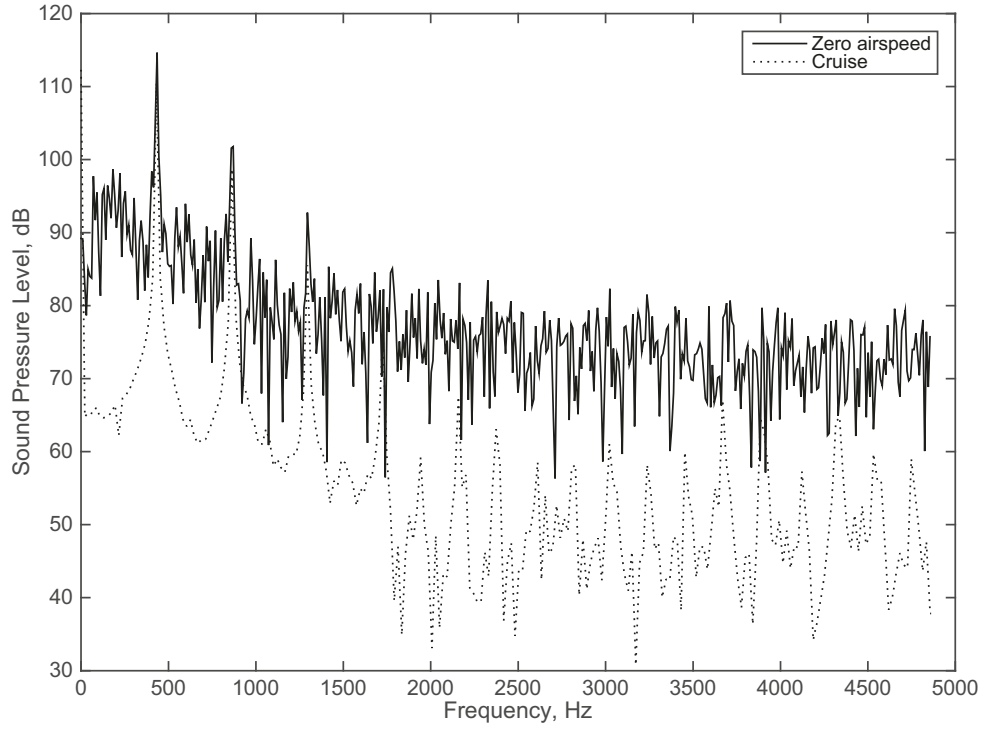


Figure 48. Acoustic spectrum at zero forward speed compared to that at cruise.

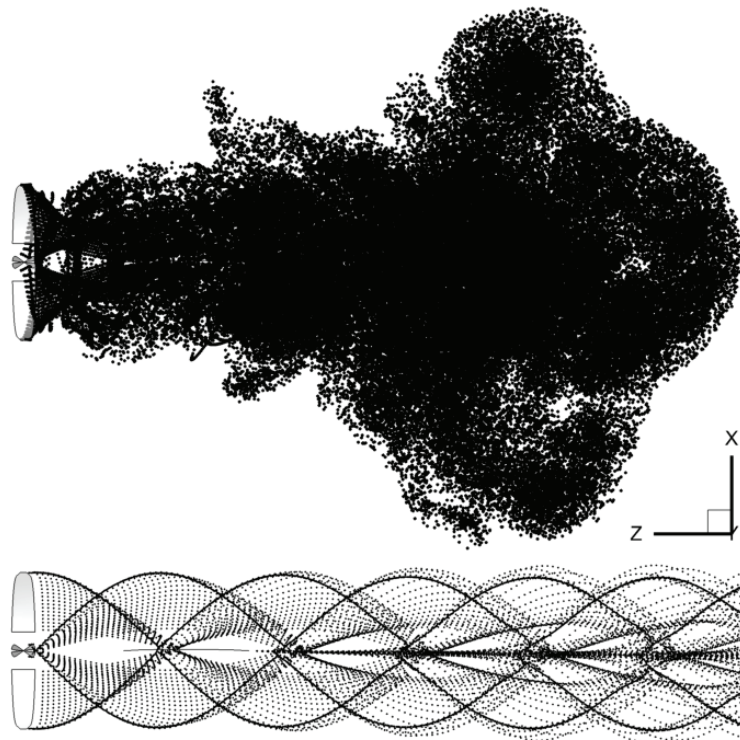


Figure 49. Particle wake structure at zero forward speed (top) and at cruise (bottom).

6. Recommendations and Conclusions

6.1. Conclusions

The present work has offered valuable insights into several aspects of the interaction noise of the combined wing/propeller system. As well as being the first research to perform numerical aeroacoustic simulations of wing vortex interaction using a vortex particle method, this was also the first research to show that local modifications of the wing's leading edge can reduce the noise of the wing-propeller system. Wing placement, nacelle presence, and off-design conditions were also investigated for the first time in this manner. SmartRotor, the numerical code used, was extended to work with blades having multiple airfoil profiles and implemented in parallel to significantly reduce computational time.

While investigating the effect of tip sweep, dihedral, and twist, it was found that forward- or aft- swept tip angles up to 60 degrees reduced tip vortex strength and left noise emission unaffected. Tip dihedral and anhedral generally increased both noise and tip vortex strength with the exception of slightly reduced tip vortex strength at around -20 degrees. Tip twist had the predictable effect of varying the tip vortex strength proportionally to tip twist angle with the proportional change in noise associated with the redistributed blade loading. In conclusion, while any of these parameters can be used to manage the strength of the tip vortex, tip sweep is the only parameter that does not also have an adverse effect on efficiency or noise.

The addition of a wing in the propeller's wake at the baseline position (in plane with the propeller axis and $0.8C$ downstream) was found to increase OASPL by 2.6 dB in this case but did not appear to affect the harmonic component. Varying the tip vortex strength relative to the wake by using more or less twisted blades showed that the change in broadband noise is a function of the wake's presence but the change in harmonic noise is correlated with tip vortex strength. Wing vertical placement was found to play a role in OASPL in that displacing the wing from the propeller's axis increased broadband noise. Harmonic noise increased slightly from the baseline case when positioned midway up or down on the propeller disc but returned to near baseline levels when at the upper or lower edge. Downstream position did not appear to have much effect on either OASPL or first harmonic SPL. For the microphone used, $1.2C$ downstream and $\pm 0.5R$ vertical placement resulted in significant harmonic noise reduction, however this is due to destructive interference at this particular microphone location.

Wing-Vortex Interaction (WVI) noise appears to function similarly to BVI noise on helicopters in that the relative angle of the vortex core and the leading edge is a strong determinant of noise. This is why broadband noise increases as the wing is moved towards the propeller disc edge as the mutual angle decreases from orthogonal. Therefore, varying the local leading edge angle to make the intersection more orthogonal when the wing must be displaced vertically (as in most tractor-configuration aircraft) is an effective method of decreasing WVI noise. While largely ineffective when the wing is in-plane with the propeller axis as the wake is already orthogonal, an OASPL

reduction up to 1 dB or a 1HSPL reduction up to 7 dB was observed under different leading edge shapes with the wing displaced vertically by $0.5R$. At the $1.0R$ position, OASPL was not reduced, but 1HSPL was reduced by up to 6 dB.

The effect of adding a nacelle and spinner was found to be very minor. Harmonic noise remained unaffected and only a slight increase in OASPL was observed. It is thus concluded that only the wing plays an important role in interference noise and that neglecting the nacelle and spinner is a reasonable approximation to reduce computational cost.

Off-design conditions such as angle of attack, yaw angle, and low speed were examined to determine their effect on the noise of the propeller/wing configuration. Increasing angle of attack was found to increase the sound pressure level of the second and higher harmonics as well as the OASPL, but left the first harmonic SPL constant. Yaw angle caused a similar proportional change in OASPL and first harmonic SPL, though with lesser magnitude. The decrease in magnitude of change is due to the changes in angle of attack exaggerating the inflow angle because of the upflow caused by the wing generating more lift.

6.2. Recommendations for Future Work

As the present work is a novel addition to the field of propeller and aircraft aeroacoustics, most recommendations for future study relate to confirming the findings discovered and ensuring they apply to other propellers and wing configurations. For example, the SR-2 propeller used throughout this research is a scaled-down propeller

designed for wind tunnel aeroacoustic testing. In scaling down the propeller, the rotational speed was increased compared to a typical full-size propeller such that the tip speed remained constant. As tip speed is a powerful determinant in propeller noise, this was a reasonable action for acoustic wind tunnel testing of propellers, however the VWI effects should be confirmed for full-scale applications.

Other recommendations relate to increasing the fidelity of the methods used. Both the wing and propeller blades were modeled as thin wings as is common practice for hybrid panel/vortex particle codes such as SmartRotor. With more time, it would be useful to simulate the baseline VWI case using a thick wing body for the wing to determine if the deflection of vortex particles around the body leads to any significant change in the acoustic field.

At the outset of this research project, it was intended to compare results from the SmartRotor code with a commercial grid-based CFD code to verify the wake structures observed as well as compare the computational efficiencies of the two methods. Due to time constraints, however, it was not possible for this to be done. Future researchers in the Rotorcraft Research Group could recreate the baseline VWI case to compare wake results between the free wake method used here and a grid-based CFD method.

Due to the large number of simulations conducted, it was necessary to choose a single location for which to compare noise results. The chosen location, in the propeller plane and above the wing, should be representative and the most useful as in the

propeller disc plane is generally the angle at which noise is a maximum. However, as seen in Section 4.4, using a single location can be prone to interference effects that may lead to non-representative values being reported. For this reason, a meta-analysis of the data from multiple locations should be conducted to ensure that the trends observed here are consistent across multiple angles of directivity.

It is also possible to extend on the current research by considering other effects such as aeroelasticity or the addition of flaps or landing gear to the full configuration. The way in which the propeller blade tips were varied in Section 3 could very easily cause them to vibrate due to aeroelastic effects which were not considered here. This additional vibration could lead to the introduction of new noise sources or reveal that some promising blade designs may not actually be feasible due to excessive stresses or vibration. This may especially be the case when the wing causes a fluctuating loading on the propeller as seen in Figure 32 of Section 4.2.

The addition of flaps to the wing, or landing gear to the engine nacelle would also affect the noise of the configuration. Landing gear is often housed in the nacelle of tractor configuration turbopropeller engines and would be a non-aerodynamic body exposed to the fluctuating flow field caused by the propeller's wake that would likely generate a significant amount of broadband noise on takeoff and landing. Flaps will also increase the non-uniformity of the propeller's inflow similar to the wing at an angle of attack and would add to both the harmonic and broadband noise through a similar mechanism.

Building on the results of the effect of wing local leading edge sweep on interaction noise by optimizing the leading edge shapes potentially holds significant scientific merit. The shapes used in this investigation were first approximations and already yielded significant harmonic noise reductions. This showed the strong potential for noise reduction and should be investigated further.

References

- [1] L. Gutin, "On the Sound Field of a Rotating Propeller," *NACA Tech. Memo.*, no. 1195, 1936.
- [2] A. F. Deming, "Propeller Rotation Noise Due to Torque and Thrust," *NACA Tech. Note*, no. 747, 1940.
- [3] M. V. Lowson, "Basic Mechanisms of Noise Generation by Helicopters, V/STOL Aircraft, and Ground Effect Machines," *J. Sound Vib.*, vol. 3, no. 3, pp. 454–466, 1966.
- [4] J. E. Marte and D. W. Kurtz, "A Review of Aerodynamic Noise from Propellers, Rotors, and Lift Fans," *NASA Tech. Rep.*, no. 32–1462, 1970.
- [5] E. D. Griffith and J. D. Revell, "Low Noise Propeller Technology Demonstration," *Air Force Aero Propuls. Lab.*, no. AD-779 773, 1974.
- [6] J. H. Dittmar and R. J. Jeracki, "Noise of the SR-3 Propeller Model at 2 and 4 Degrees Angle of Attack," *NASA Tech. Memo.*, no. 82738, 1981.
- [7] J. H. Dittmar, G. L. Stefko, and R. J. Jeracki, "Noise of the SR-6 Propeller Model at 2 and 4 Degrees Angles of Attack," *NASA Tech. Memo.*, no. 83515, 1983.
- [8] W. Dobrzynski, H. Heller, J. Powers, and J. Densmore, "Propeller Noise Tests in the German-Dutch Wind Tunnel DNW," *FAA Rep.*, no. AEE 86-3, 1986.
- [9] J. H. Dittmar, "Cruise Noise of the SR-2 Propeller Model in a Wind Tunnel," *NASA Tech. Memo.*, no. 101480, 1989.
- [10] M. Carley, "Propeller Noise Fields," *J. Sound Vib.*, vol. 233, no. 2, pp. 255–277, 2000.
- [11] T. Theodorsen and A. A. Regier, "The Problem of Noise Reduction with Reference to Light Airplanes," *NACA Tech. Note*, no. 1145, 1948.
- [12] F. B. Metzger, "An Assessment of Propeller Aircraft Noise Reduction Technology," *NASA Contract. Rep.*, no. 198237, 1995.
- [13] F. B. Metzger, "A review of propeller noise prediction methodology: 1919-1994," *NASA Contract. Rep.*, no. 198156, 1995.
- [14] P. T. Soderman and W. C. Horne, "Acoustic and Aerodynamic Study of a Pusher-Propeller Aircraft Model," *NASA Tech. Pap.*, no. 3040, 1990.
- [15] E. A. Krejsa, "Prediction of the Noise from a Propeller at Angle of Attack," *NASA*

Tech. Memo., no. 103627, 1990.

- [16] M. S. Ryerson and M. Hansen, "The potential of turboprops for reducing aviation fuel consumption," *Transp. Res. Part D Transp. Environ.*, vol. 15, no. 6, pp. 305–314, 2010.
- [17] T. Dwyer, "Assessing and improving the acoustic performance of soil and waste pipes in buildings," *CIBSE Journal*, 2016. [Online]. Available: <http://www.cibsejournal.com/cpd/modules/2016-05-aco/>. [Accessed: 13-Jun-2016].
- [18] J. F. Unruh, "Installation effects on propeller wake/vortex induced structure-borne noise transmission," *J. Aircr.*, vol. 27, no. 5, pp. 444–448, 1990.
- [19] B. A. Miller, J. H. Dittmar, and R. J. Jeracki, "Propeller Tip Vortex: A Possible Contributor to Aircraft Cabin Noise," *NASA Tech. Memo.*, no. 81768, 1981.
- [20] D. B. Hanson, "Influence of Propeller Design Parameters on Far-Field Harmonic Noise in Forward Flight," *AIAA J.*, vol. 18, no. 11, pp. 1313–1319, 1980.
- [21] F. B. Metzger and C. Rohrbach, "Benefits of blade sweep for advanced turboprops," *21st AIAA/SAE/ASME/ASEE Jt. Propuls. Conf.*, vol. 2, no. 6, pp. 1–11, 1985.
- [22] L. K. Chang and J. P. Sullivan, "Optimization of Propeller Blade Twist by an Analytical Method," *AIAA J.*, vol. 22, no. 2, pp. 252–255, 1984.
- [23] J. Cho and S.-C. Lee, "Propeller blade shape optimization for efficiency improvement," *Comput. Fluids*, vol. 27, no. 3, pp. 407–419, 1998.
- [24] J. F. Unruh, "Aircraft propeller induced structure-borne noise," *NASA Contract. Rep.*, no. 4255, 1989.
- [25] J. F. Unruh, "Simulation and Control of Propeller Induced Structure-Borne Noise," *Noise Control Eng. J.*, vol. 36, no. 2, pp. 91–96, 1991.
- [26] P. A. Durbin and J. F. Groeneweg, "Rough Analysis of Installation Effects on Turboprop Noise," *NASA Tech. Memo.*, no. 82924, 1982.
- [27] A. A. Rangwalla and L. N. Wilson, "Application of a panel code to unsteady wing-propeller interference," *J. Aircr.*, vol. 24, no. 8, pp. 568–571, 1987.
- [28] G. Fratello, D. Favier, and C. Maresca, "Experimental and Numerical Study of the Propeller/Fixed Wing Interaction," *J. Aircr.*, vol. 28, no. 6, pp. 365–373, 1991.
- [29] R. M. A. Marretta, "Different Wings Flowfields Interaction on the Wing-Propeller

- Coupling," *J. Aircr.*, vol. 34, no. 6, pp. 740–747, 1997.
- [30] R. M. A. Marretta, G. Davi, G. Lombardi, and A. Milazzo, "Hybrid numerical technique for evaluating wing aerodynamic loading with propeller interference," *Comput. Fluids*, vol. 28, no. 8, pp. 923–950, 1999.
- [31] R. M. A. Marretta, G. Davi, A. Milazzo, G. Lombardi, and M. Carley, "Simulation Model and Computation of Noise Emission of an Installed Propeller," *Comput. Model. Simul. Eng.*, vol. 4, no. 2, pp. 104–116, 1999.
- [32] R. A. D. Akkermans, M. Pott-Pollenske, H. Buchholz, J. W. Delfs, and D. Almonet, "Installation Effects of a Propeller Mounted on a High-Lift Wing with a Coanda Flap. Part I: Aeroacoustic Experiments," *20th AIAA/CEAS Aeroacoustics Conf.*, no. June, pp. 1–15, 2014.
- [33] V. Clair, C. Polacsek, T. Le Garrec, G. Reboul, M. Gruber, and P. Joseph, "Experimental and Numerical Investigation of Turbulence-Airfoil Noise Reduction using Wavy Edges," *AIAA J.*, vol. 51, no. 11, pp. 2695–2713, 2013.
- [34] M. Roger, C. Schram, and S. Moreau, "On vortex-airfoil interaction noise including span-end effects, with application to open-rotor aeroacoustics," *J. Sound Vib.*, vol. 333, no. 1, pp. 283–306, 2014.
- [35] M. J. Kingan and R. H. Self, "Counter-Rotation Propeller Tip Vortex Interaction Noise," in *15th AIAA/CEAS Aeroacoustics Conference*, 2009.
- [36] R. H. Welge, D. H. Neuhart, and J. A. Dahlin, "Analysis of Mach Number 0.8 Turboprop Slipstream Wing/Nacelle Interactions," *NASA Contract. Rep.*, 1981.
- [37] H. K. Tanna, R. H. Burrin, and H. E. Plumbree, "Installation effects on propeller noise," *J. Aircr.*, vol. 18, no. 4, pp. 303–309, 1981.
- [38] S. Morrell, R. Taylor, and D. Lyle, "A review of health effects of aircraft noise," *Aust N Z J Public Heal.*, vol. 21, no. 2, pp. 221–236, 1997.
- [39] S. Cohen, G. W. Evans, D. S. Krantz, and D. Stokols, "Physiological, motivational, and cognitive effects of aircraft noise on children: moving from the laboratory to the field.," *Am. Psychol.*, vol. 35, no. 3, pp. 231–243, 1980.
- [40] D. G. Opoku, D. G. Triantos, F. Nitzsche, and S. G. Voutsinas, "Rotorcraft Aerodynamic and Aeroacoustic Modelling Using Vortex Particle Methods," *ICAS 2002 Congr.*, p. 299.1-299.11, 2002.
- [41] M. G. Martin, "Articulated Rotor Hub Model for 3D Aeroelastic Simulation of Helicopter Rotors by," M.A.Sc thesis, Dept. Mech. and Aero. Eng., Carleton Univ., Ottawa, Canada, 2011.

- [42] D. G. Opoku, "Aeroelastic and Aeroacoustic Modelling of Rotorcraft," M.A.Sc thesis, Dept. Mech. and Aero. Eng., Carleton Univ., Ottawa, Canada, 2002.
- [43] F. Nitzsche and D. G. Opoku, "Acoustic Validation of a New Code Using Particle Wake Aerodynamics and Geometrically-Exact Beam Structural Dynamics," *Aeronaut. J.*, vol. 109, no. 6, pp. 257–267, 2005.
- [44] M. De Gennaro, D. Caridi, and M. Pourkashanian, "Ffowcs Williams-Hawkings Acoustic Analogy for Simulation of Nasa SR2 Propeller Noise in Transonic Cruise Condition," *V Eur. Conf. Comput. Fluid Dyn.*, vol. 1281, no. 1, p. 167, 2010.
- [45] V. A. Riziotis and S. G. Voutsinas, "Modelling of Wind Tunnel Interference on Helicopter Measurements and Assessment of the Currently Used Corrections Based on the HeliNoVi Database," *32nd Eur. Rotorcr. Forum*, pp. 408–427, 2006.
- [46] H. Abedi, L. Davidson, and S. G. Voutsinas, "Vortex Method Application for Aerodynamic Loads on Rotor Blades," *Eur. Wind Energy Event 2013*, vol. 2, pp. 912–921, 2013.
- [47] H. Abedi, L. Davidson, and S. G. Voutsinas, "Enhancement of free vortex filament method for aerodynamic loads on rotor blades," *ASME 2014 Int. Mech. Eng. Congr. Expo.*, p. C11, 2014.
- [48] J. L. Hess and A. M. O. Smith, "Calculation of Non-Lifting Potential Flow About Arbitrary Three-Dimensional Bodies," *McDonnell Douglas Tech. Rep.*, no. E.S. 40622, 1962.
- [49] J. L. Hess, "Calculation of Potential Flow About Arbitrary Three-Dimensional Lifting Bodies," *McDonnell Douglas Tech. Rep.*, no. MDC J5679-01, 1972.
- [50] S. G. Voutsinas and D. G. Triantos, "High-resolution Aerodynamic Analysis of Full Helicopter Configurations," in *Proceedings of the 25th European Rotorcraft Forum*, 1999.
- [51] J. Katz and A. Plotkin, *Low-Speed Aerodynamics*. New York, NY: Cambridge University Press, 2001.
- [52] J. T. Beale and A. Majda, "High Order Accurate Vortex Methods with Explicit Velocity Kernels," *J. Comput. Phys.*, vol. 58, pp. 188–208, 1985.
- [53] K. S. Brentner and F. Farassat, "Analytical Comparison of the Acoustic Analogy," *AIAA J.*, vol. 36, no. 8, pp. 1379–1386, 1998.
- [54] H. H. Hubbard, "Aeroacoustics of Flight Vehicles - Theory and Practice," *NASA Ref. Publ.*, vol. 1, no. 1258, pp. 89–94, 1991.

- [55] MathWorks, "Fast Fourier Transform (fft)," *MATLAB Documentation*, 2016. [Online]. Available: <http://www.mathworks.com/help/matlab/math/fast-fourier-transform-fft.html>. [Accessed: 16-Aug-2016].
- [56] J. Wiebe, "Development of a Simulation and Optimization Framework for Improved Aerodynamic Performance of R / C Helicopter Rotor Blades," M.A.Sc. thesis, Dept. Mech. and Aero. Eng., Carleton University, Ottawa, Canada, 2015.
- [57] K. S. Brentner and F. Farassat, "Modeling aerodynamically generated sound of helicopter rotors," *Prog. Aerosp. Sci.*, vol. 39, no. 2, pp. 83–120, 2003.
- [58] C. J. Doolan, F. N. Coton, and R. A. M. Galbraith, "The Effect of a Preceding Blade on the Orthogonal Vortex Interaction," *J. Am. Helicopter Soc.*, vol. 46, no. 3, pp. 221–227, 2001.
- [59] Norebbo, "Q400 Line Drawing," 2015. [Online]. Available: <http://www.norebbo.com/2015/08/bombardier-dhc-8-402-q400-blank-illustration-templates/>. [Accessed: 18-May-2016].